ECAP-2021

Ray Tracing Simulation for Astro Quantum Optics

Master's Thesis in Physics

Presented by
Sebastian Konrad
04.05.2021

Erlangen Centre for Astroparticle Physics
Friedrich-Alexander-Universität Erlangen-Nürnberg

1. Supervisor: Prof. Dr. Stefan Funk
2. Supervisor: Prof. Dr. Gisela Anton

Abstract

Intensity interferometry can be used to gain information about the geometry of stars especially their angular size. The intensity fluctuations of a thermal light source like stars are not random, but correlated. This correlation can be measured by simultaneous detection of light from the source at different locations. Unlike amplitude interferometries, where precise optics is needed to make an interference pattern, intensity interferometries maximal baseline is not limited to a few hundred meters by atmospheric disturbances of the light. The possibility of larger baselines promises not yet seen angular resolution of sub-milliarcseconds in the optical range.
The first optical stellar intensity interferometer was developed by Hanbury Brown and Twiss in the 1950s [1] and later improved in the Narrabri stellar interferometer which was able to measure a catalog of 32 bright stars [2]. The needed challenging time resolution to detect the correlation peak of the signal prohibited further development to this kind of measurement to this day. However today improved electronics make this technique feasible. In addition to that available existing gamma ray telescopes that can be used for optical interferometry provide a good opportunity to revive this method.

This thesis uses ray tracing simulations to characterize two planned different interferometry experiments. For the H.E.S.S. telescopes the simulations are used to optimize a specifically designed interferometry setup by changing lenses and their positions regarding the focal point of the telescope. This varies the angles of incidence (AOIs) on an interference filter and hence the transmission spectrum. IceAct simulation focuses on the properties of the used Fresnel lens and its impact on the measured spectrum.

Contents

1 Stellar interferometry

1.1 Interference

The famous double-slit experiment by Thomas Young was early evidence that light can be described as waves. As later confirmed by quantum mechanics the hypothesis of light as wave was partially correct. This means light shows interference behavior. In the double-slit experiment, light is emitted on two narrow slits and detected afterwards (see Figure 1.1).

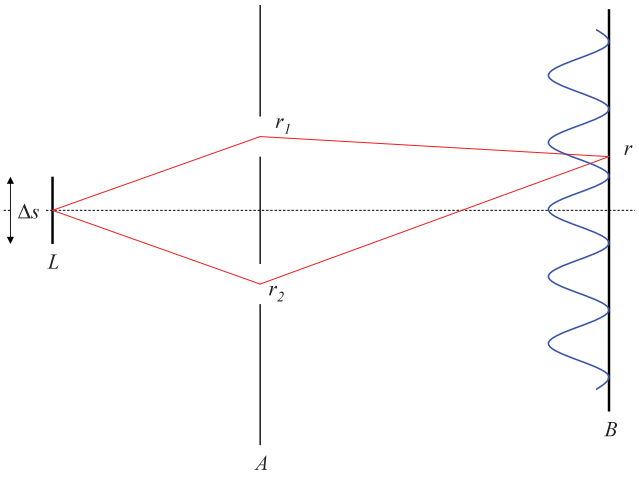

Figure 1.1: Double-slit with slits r_1 and r_2 and lateral width Δs with produced interference pattern [3]

To calculate the electrical field $\tilde{E}(r,t)$ in dependence of time t and location r the superposition of the two single fields can be used:

$$\begin{aligned} \tilde{E}(r,t) &= E_1(r,t) + E_2(r,t) \\ = E_1(r_1, t - \frac{r - r_1}{c}) &+ E_2(r_2, t - \frac{r - r_2}{c}) \\ &= E_1(r_1,t) + E_2(r_2, t+\tau)[3] \end{aligned} \tag{1.1}$$

with the run time difference $\tau = \frac{|r_2 - r| - |r_1 - r|}{c}$ between the rays from slit r_1 and r_2. An interference pattern is only formed if there is a temporal or spatial fixed phase relation between the waves. There are different effects that can disturb this phase relation:

- the frequency changes over time
- the light source is sending finite wave trains with statistical distributed phases
- the refractive index changes between source and observer over time [3]

The maximal time period Δt_c in which the phase difference between all partial waves in a point does not increase greater than 2π is called coherence time [4, p. 286]. However this is just one definition of coherence time. Later on coherence time is going to be defined as the integral of the $g^{(2)}$ function.
The temporal overlay of two partial waves is illustrated in Figure 1.2.

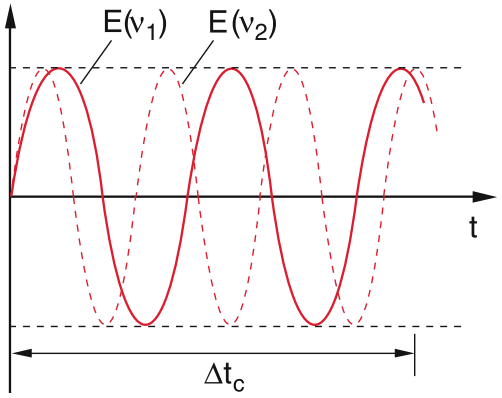

Figure 1.2: Temporal overlay of two partial waves [4, p. 286]

The coherence time can be described by:

$$\Delta t_c \propto \frac{1}{\Delta \nu} [4, \text{ p. } 286] \tag{1.2}$$

where $\Delta \nu$ is the width of the frequency spectrum. This means the spectral width is a key element in a measurement setup where coherence is used.

1.2 Correlation of first order

Equation 1.1 describes the electric field. The intensity is given by:

$$I(r,t) \propto \left|\tilde{E}(r,t)\right|^2 = |E_1(r_1,t)|^2 + |E_2(r_2,t+\tau)|^2 + 2\Re[E_1^*(r_1,t)E_2(r_2,t+\tau)].[3] \tag{1.3}$$

Under the assumption of equal amplitudes $E_1(r_1,t) = E_2(r_2,t+\tau)$ it leads to the intensity correlation function of first order:

$$g^{(1)}(r_1,r_2,\tau) = \frac{\langle E^*(r_1,t)E(r_2,t+\tau)\rangle}{\langle E^*(r_1,t)E(r_1,t)\rangle} [3] \tag{1.4}$$

For $r_1 = r_2$ the $g^{(1)}$ is called temporal correlation function of first order $g^{(1)}(\tau)$. For $\tau = 0$ it is called spatial correlation function of first order $g^{(1)}(r_1,r_2)$

1.2.1 Wiener-Khintchine Theorem

The temporal correlation function of first order informs about how much light from a light source is correlated in time. This also bears information about the

spectral intensity distribution of the used light source [3]. This relation is given by the Wiener-Khintchine Theorem.
The theorem can be derived by Fourier Transform of the electrical field:

$$E(\omega) = \frac{1}{\sqrt{2\pi}} \int_{-\infty}^{+\infty} E(t) e^{i\omega t} dt [3] \tag{1.5}$$

The intensity is then given by:

$$\begin{aligned} I = |E(\omega)|^2 &= \frac{1}{2\pi} \int_{-\infty}^{\infty} \int_{-\infty}^{\infty} E^*(t) E(t') e^{i\omega(t'-t)} dt dt' \\ &\overset{\tau = t'-t}{=} \frac{1}{2\pi} \int_{-\infty}^{\infty} \int_{-\infty}^{\infty} E^*(t) E(t+\tau) e^{i\omega(\tau)} dt d\tau \\ &\overset{\langle E^*(t)E(t+\tau)\rangle = \frac{1}{T}\int_T E^*(t)E(t+\tau)dt}{=} \frac{T}{2\pi} \int_{-\infty}^{+\infty} \langle E^*(t) E(t+\tau) \rangle e^{i\omega\tau} d\tau [3] \end{aligned} \tag{1.6}$$

Note that $\langle E^*(t)E(t+\tau)\rangle$ is equivalent to the autocorrelation function [5, p. 429]. If this gets normalized, it leads to:

$$F(\omega) = \frac{T}{2\pi} \int_{-\infty}^{+\infty} \frac{\langle E^*(t)E(t+\tau)\rangle e^{i\omega\tau}}{\langle E^*(t)E(t)\rangle} d\tau = \frac{1}{2\pi} \int_{-\infty}^{+\infty} g^{(1)}(\tau) e^{i\omega\tau} d\tau [3]. \tag{1.7}$$

The connection of $g^{(1)}(\tau)$ with $F(\omega)$ by Fourier Transform also means that τ_c and the spectral width of the source $\Delta\nu$ are inversely proportional to each other (see Equation 1.2).

1.2.2 Van-Cittert-Zernike Theorem

Besides the relation between the correlation function $g^{(1)}(\tau)$ and the spectrum of the source there is also a relation between the correlation function and the geometry of the source (the spatial intensity distribution). In this case not the temporal but the spatial correlation function $g^{(1)}(r_1, r_2)$ is used. The Van-Cittert-Zernike Theorem can only be used under following assumptions:

- the source is incoherent.
- the distance to the source is sufficiently greater than the size of observation area, so that a far field approximation can be used.
- the source is close to being monochromatic, so that the coherence time is sufficently large [3].

For the far field expression of the correlation function, the two dimensional Fourier Transform of the spatial correlation function has to be taken and has to be normalized:

$$g^{(1)}(\mathbf{r_1}, \mathbf{r_2}) = e^{ik(r_2 - r_1)} \frac{\int_\sigma I(\mathbf{r}') e^{-ik[(s_2 - s_1)r']} d^2\mathbf{r}'}{\int_\sigma I(\mathbf{r}') d^2\mathbf{r}'} [3] \tag{1.8}$$

where $r_j = |\mathbf{r_j}|$ is the distance to the source to $\mathbf{r_j} = r_j s_j$ with the unit vector s_j in the direction to r_j. σ is the geometry of the light source with the intensity

distribution $I(\mathbf{r}')$. If this relation is applied on a circular aperture, it leads to an Airy pattern:

$$g^{(1)}(r_1, r_2) = \frac{2J_1(X)}{X} \text{ with } X = \frac{\pi a(r_2 - r_1)}{R\lambda} [3] \tag{1.9}$$

with a the diameter of the aperture and the distance from source to detector R and J_1 the first order Bessel function.
This means that there is a connection between the geometry of a source and its correlation function which can be used to get information about the source. Even if it would not be possible to measure an angular diameter with classical telescopes due to its small size.
This can only be done because of the fact that a light source of certain shape produces the same correlation as its complementary aperture (a slit of the same certain shape). It is a circular aperture for a circular light source. The equivalent behaviour of light source and its complementary aperture is given by Babinet's principle [4, p. 317].

1.2.3 Michelson interferometer

The Michelson interferometer uses the previously shown properties and relations to function as a stellar double-slit interferometer. It consists out of a telescope with a double-slit or two or more telescopes (see Figure 1.3).

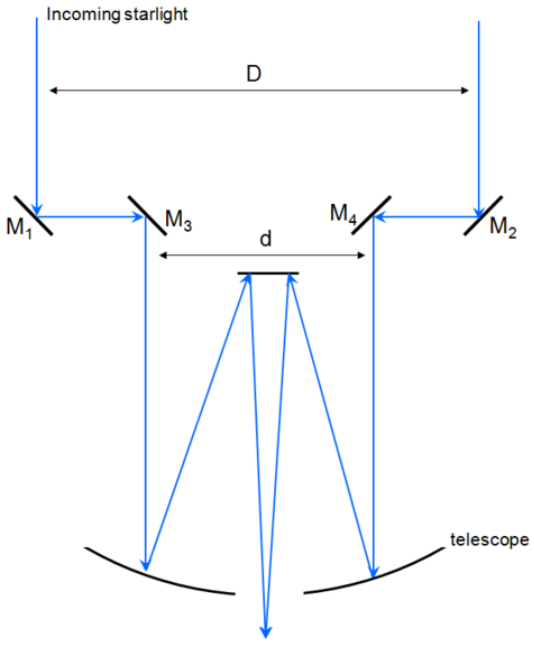

Figure 1.3: Illustration of a Michelson interferometer with the baseline distance D and double-slit size d [6]

If a light ray with an angle hits a double-slit, a path difference is produced compared to a light ray without this angle (see Figure 1.4) given by:

$$\Delta S = D \cdot (\sin\theta - \sin\theta') \overset{\text{small-angle approximation}}{=} D \cdot (\theta - \theta')[7] \tag{1.10}$$

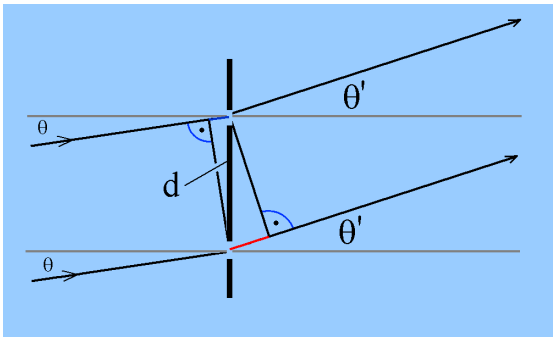

Figure 1.4: Illustration of the path difference at the double-slit for different angles [7]

A point-like source would give a classical interference pattern, but for an extent source, like a star every point on the surface produces its own interference pattern. This extent can not be resolved classically, but the superposition of the interference patterns can be obsolved.
For the first point-like source 1 a maximum in the interference pattern is given by:

$$\Delta S_1 = D \cdot (\theta_1 - \theta') = k \cdot \lambda \overset{\text{for max: } k=1}{=} \lambda[7] \tag{1.11}$$

If a minimum of another point-like source 2 is on the same spot as the maximum, the interference pattern disappears. The minimum of the second source is given by:

$$\Delta S_2 = D \cdot (\theta_2 - \theta') = \lambda/2[7] \tag{1.12}$$

Equation 1.11 and 1.12 combined lead to:

$$\begin{aligned} D \cdot (\theta_1 - \theta') &= 2D \cdot (\theta_2 - \theta') = \lambda \\ \Rightarrow \Delta\theta = \theta_1 - \theta_2 &= \frac{\lambda}{2D}[7] \end{aligned} \tag{1.13}$$

Note that $\Delta\theta$ is not the stellar diameter, but the angular diameter of the star. In practice one starts with a small baseline and increases it until the interference pattern disappears. This means the resolution does not depend on the size and precession of the optics, but mostly on the maximal baseline.
The Michelson interferometer is classified as an amplitude interferometer because it uses optical interference of the amplitude of the light.
Precise optics is needed, especially for large baselines, since the margin of error has to be smaller than $\lambda/2$ to successfully match a minimum with a maximum. In practice such a measurement is normally located in the radio regime because unlike optical light the radio frequency is more stable against atmospheric disturbance. Also active and adaptive optics are needed for big baselines to get the light to interfere without any time difference.
A way to deal with that issue is using intensity interferometry instead of amplitude interference.

1.3 Correlation of second order

The first order correlation function is hard to measure directly for optical light. Therefore one needs another description of correlation that can be measured easier and is related to the first order correlation. This description is the second order correlation function:

$$g^{(2)}(r_1, r_2, \tau) = \frac{\langle E^*(r_1,t)E^*(r_2,t+\tau)E(r_2,t+\tau)E(r_1,t)\rangle}{\langle E^*(r_1,t)E(r_1,t)\rangle \langle E^*(r_2,t)E(r_2,t)\rangle} \tag{1.14}$$

$$= \frac{\langle I(r_1,t)I(r_2,t+\tau)\rangle}{\langle I(r_1,t)\rangle \langle I(r_2,t)\rangle}[3] \tag{1.15}$$

$g^{(2)}(r_1, r_2, \tau)$ depends on the intensity of two different spots r_1 and r_2. Since intensities can be measured easily this description is useful for a possible measurement setup.

1.3.1 Siegert Relation

The relation linking the first order correlation with the second order correlation for thermal light is called Siegert relation. It is given by:

$$g^{(2)}(r_1, r_2, \tau) = 1 + \left|g^{(1)}(r_1, r_2, \tau)\right|^2 [3]. \tag{1.16}$$

In combination with Equation 1.9 this leads to:

$$g^{(2)}(r_1, r_2) = 1 + \left|\frac{2J_1(X)}{X}\right|^2 \tag{1.17}$$

for a circular aperture.

1.3.2 Hanbury Brown-Twiss experiment

An example for an optical intensity interferometer was the Hanbury Brown-Twiss experiment in Narrabri, Australia (see Figure 1.5).
In intensity interferometry the light is not collected at different places and then brought together to interfere, but the amount of arriving photons (intensity) is measured and can then be correlated afterwards, which can be done digitally. This means that the data of each telescope, or just a light detector, for example a light collector with a photomultiplier tube (PMT), can be measured with a good time resolution and then be saved and there is no need for complex optics like adaptive or active optics. Nonetheless if the bandwidth of the spectrum is large the time to measure a significant signal becomes increasingly big. One solution is to narrow down the bandwidth by using a bandpass filter.
The Narrabri Observatory consisted out of two large mosaic reflectors with a diameter of 6.7m mounted on a circular railway track with 188m diameter, which allowed the reflectors to have different distances (baselines) between 10-188m to each other. From the reflectors the light was reflected into a narrow-band interference filter and then focused into a PMT[2].
To make the measurement a baseline is chosen and then the number of coincident

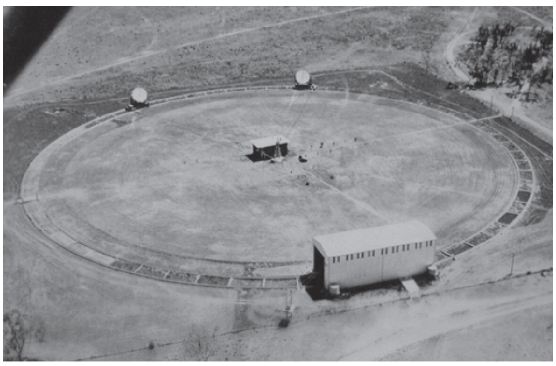

Figure 1.5: Picture of the Narrabri stellar interferometer [1]

photons arriving at both PMTs are counted. After that the baseline is changed and measured again. If this is done for multiple baselines, one can construct the $g^{(2)}$ correlation functions out of the intensity measurements (see Figure 1.6).

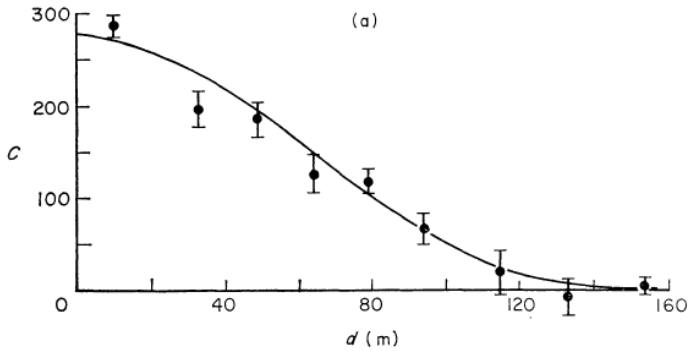

Figure 1.6: Observed variation of correlation c with different baselines d of β Cru measured at the Narrabri stellar interferometer [8]

In the Narrabri Observatory the different baselines where realized by having the light detectors on rail, so that they can be moved relatively to each other.
For bigger and more complex telescopes a rail system is not practicable, but intensity interferometry is still possible. That is the case because the Earth is rotating and with this rotation the light propagates from different angles into the setup, which changes the projected baseline (see Figure 1.7). So even if the distance between the telescopes does not change, the actual baseline changes over time.

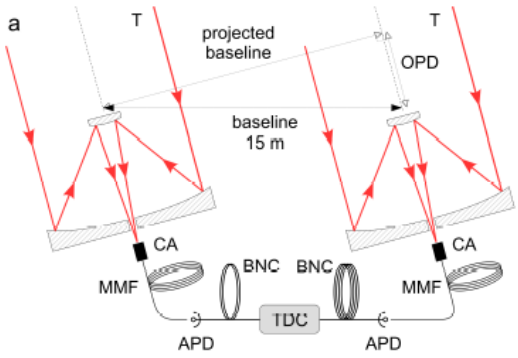

Figure 1.7: Illustration of a projected baseline[9]

2 Simulation of optics

The simulation technique used in this thesis is called ray tracing. It is a procedure based on geometric optics. Therefore the basic axioms of geometrical optics apply [4, p. 250]:

- In an optical homogeneous medium light rays are straight lines.
- At the boundary between two media light beams are refracted according to Snell's law: $\frac{\sin\alpha}{\sin\beta} = \frac{c_1'}{c_2'} = \frac{n_2}{n_1}$[4, p. 222].
- Rays that traverse each other do not influence each other within the framework of linear optics.

The form of ray tracing chosen is sequential ray tracing. The basic idea is that the simulation starts with a bundle of initial light rays and propagates those through the optics step by step. In between the optical devices the rays propagate in straight lines. Only the intersection of the rays with the optical device has to be calculated. After that the rays get transformed according to the specific optical component[10].

3 Intensity interferometry with H.E.S.S.

3.1 Optics used in H.E.S.S. for intensity interferometry

The High Energy Stereoscopic System (H.E.S.S.) is an Air Cherenkov telescope array mainly used for high energy gamma ray astronomy in Namibia. The Cherenkov light, which is emitted in these air showers, is in the visible spectrum. Therefore the whole telescope setup is optimized to measure in the visible range. Especially favorable is the fact, that the telescopes can just be used for gamma ray astronomy under certain light conditions. For example if it is full moon it is not possible to do gamma ray astronomy. The same is true for all other situations where there is much stray light.
This leaves time windows open for intensity interferometry measurements. The telescopes that are planned to be used for intensity interferometry are the 12 m telescopes of the H.E.S.S. site (see Figure 3.1).

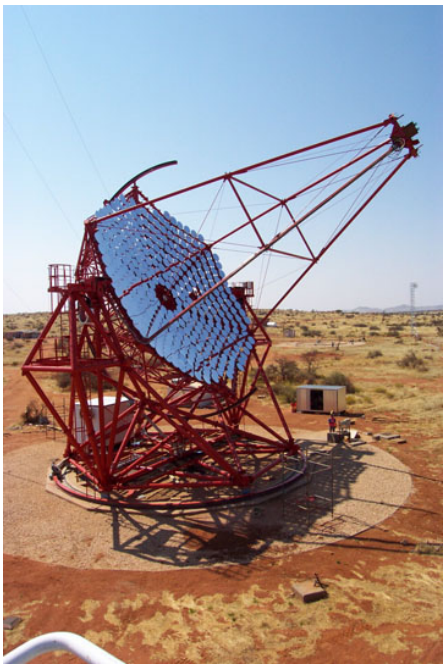

Figure 3.1: Picture of the 12m H.E.S.S. telescope on the Namibia site [11]

The mirror dish of the telescope consists of 382 60 cm sized mirrors which focus the incoming light onto the camera which is located at the end of the mount and which is facing the dish (see Figure 3.2). The mirrors have got a total area of 108 m^2 and focal length of 15 m while the diameter of the mirrors on the dish is 12 m [12]. The pointing of the telescope is assured by a charge-coupled device (CCD) camera, which is located in the middle of the mirror dish.
The interferometry setup consists of a 45° mirror, two lenses, an interference filter (and a beam splitter for the zero baseline measurement) as well as a photon detector and is planned to be installed on the camera lid of the telescope (see Figure 3.3).

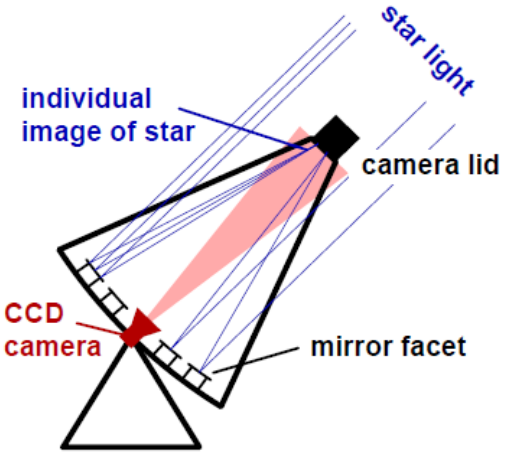

Figure 3.2: Illustration of the functionality of the H.E.S.S. 12 m telescope[13]

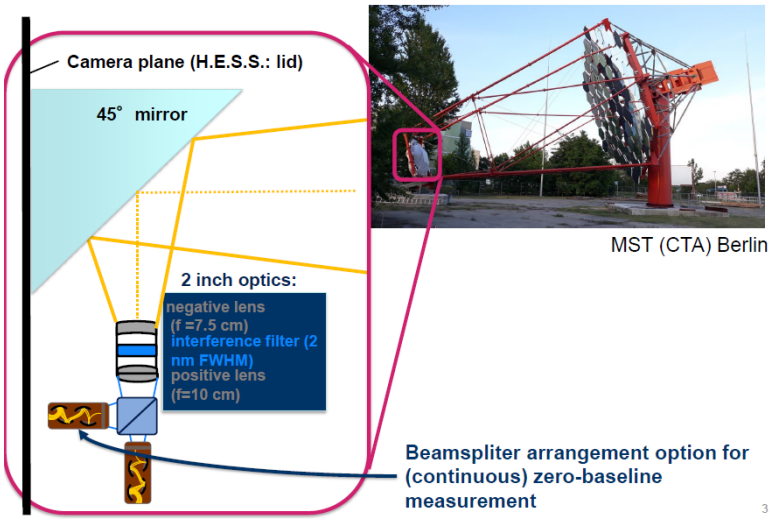

Figure 3.3: Depiction of the intensity interferometry setup mounted onto a telescope [14]

This is done so it can quickly be switched between the two setups and also that the gamma astronomy camera is secure from too much light exposure during the interferometry measurements.
As a photon detector a 23 mm x 23 mm Hamamatsu R11265U PMT is used [15]. The general size of the used optics is 2 inches in diameter which corresponds to 5.08 cm.

3.1.1 Interference filter

Interferometry is hardly possible for big bandwidth especially for thermal light, because for these light sources the fixed phase relation and therefore also the correlation time τ_c (see section 1.1) are small. This can be solved by narrowing the bandwidth with a bandpass filter. The filter used in the H.E.S.S. setup is an interference filter. An example for the almost rectangular shape of the spectrum produced by an interference filter is demonstrated in Figure 3.4.
An interference filter consists of multiple layers of reflecting and transmitting materials. One of such a layer is shown in Figure 3.5. The concept of the filter is that incoming light rays get reflected in between the layers of the highly reflective, but still semireflective, material multiple times and only interfere constructive inside the layers if the wavelength is:

$$\lambda_m = \frac{2d}{m}\sqrt{n^2 - \sin^2\alpha}\text{[16, p. 92]} \tag{3.1}$$

with λ_m the wavelength of the transmission maximum of m-th order with the angle θ of the incoming light onto the filter.
For all other wavelengths the interference is destructive. The used filters in the setup are so called narrow bandpass filters. These can be produced by using three reflective layers with intervening dielectric spacer layers [16, p. 103] and are characterized by their steep flanks.

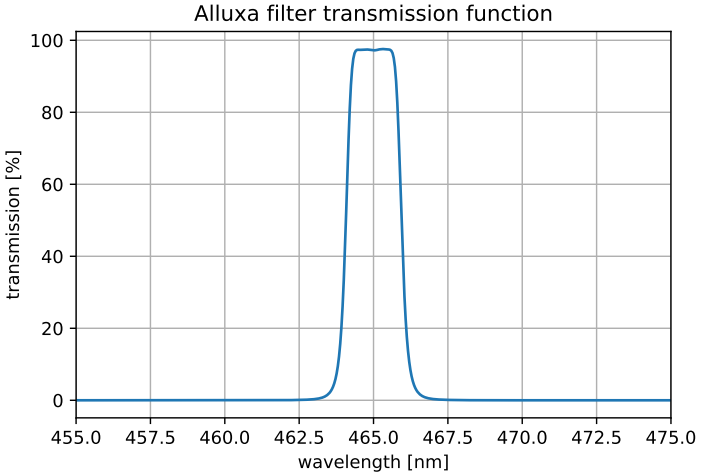

Figure 3.4: Example of a transmission function of an interference filter from Alluxa with bandwidth 2 nm and a center wavelength 465 nm [17]

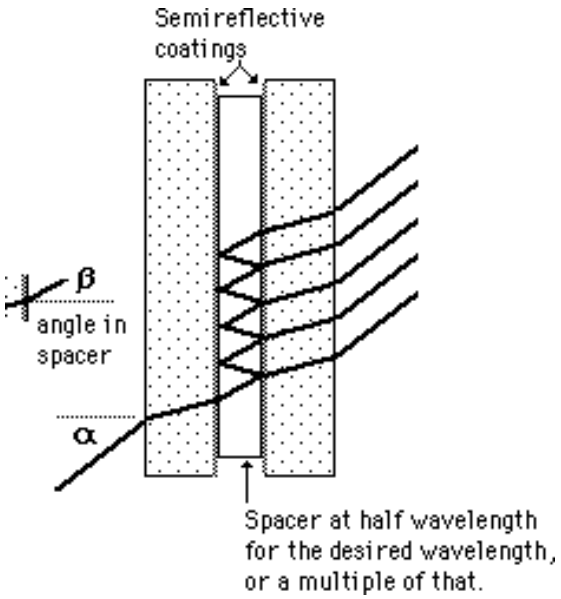

Figure 3.5: Illustration of the functionality of an interference filter [18]

The transmission wavelengths are quite dependent on the AOI of the incoming rays. This is described with the following Equation 3.2:

$$\lambda_\theta = \lambda_0 \sqrt{1 - \left(\frac{n_0}{n_{\text{eff}}} \sin\theta\right)^2} \text{[19]} \tag{3.2}$$

with:
λ_θ = wavelength corresponding to the feature of interest at incident angle θ
λ_0 = wavelength corresponding to the feature of interest at normal incidence
n_0 = refractive index of incident medium
n_{eff} = effective refractive index of the optical filter
θ = angle of incidence
This formula leads to its trivial version if the AOI is 0°:

$$\lambda_\theta = \lambda_0 \sqrt{1 - \left(\frac{n_0}{n_{\text{eff}}} \sin 0°\right)^2} = \lambda_0 \tag{3.3}$$

If greater AOIs are plugged in, the wavelength shifts to smaller values. This behavior is pictured in Figure 3.6 for the same example filter as in Figure 3.4. The AOI dependence of the interference filter is important for the intensity interferometry measurements because the H.E.S.S. telescopes' mirrors focus the incoming light on a focal plane. That means that the light rays' trajectories onto the intensity interferometry setup are not parallel to each other, but come in with an angle to the optical axis. Therefore the AOIs are not zero. If many rays with different AOIs hit the filter, the produced spectrum will widen (see Figure 3.7) and therefore change interferometry properties. To get a spectrum that is as narrow as possible, the spread of AOIs has to be as small as possible.
Three interference filters, which were investigated in this thesis are pictured in Figure 3.8, 3.9 and 3.10. These interference filters have a different bandwidth with 2 nm, 8.2 nm and 10 nm.

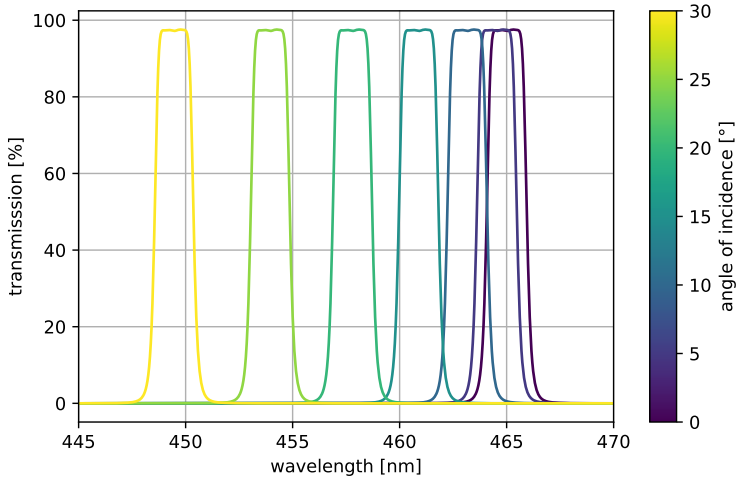

Figure 3.6: Shift of the filter spectrum to smaller wavelengths because of greater AOIs

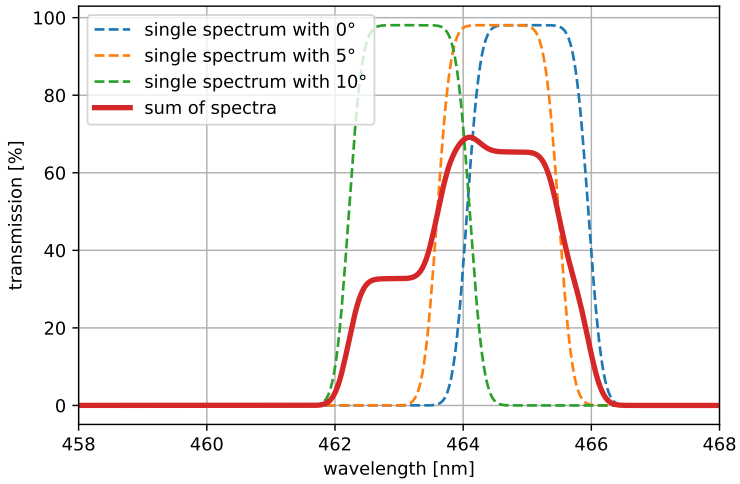

Figure 3.7: Visualization of spectra with different AOIs add up to a combined spectrum

A bigger bandwidth corresponds (as can be seen in Equation 1.2) to a smaller correlation time. So the initial thought might be that there is no reason to use a filter with a bigger bandwidth, but if the bandwidth is small and the AOIs are big, the combined spectrum might be discontinous with bands where there is less intensity, but this means that photons on both sides of this band gap can not interfere with each other. This can be prevented with a bigger bandwidth which smears out this effect. An additional effect that is prevented that way is the shift of the central wavelength to smaller wavelengths.

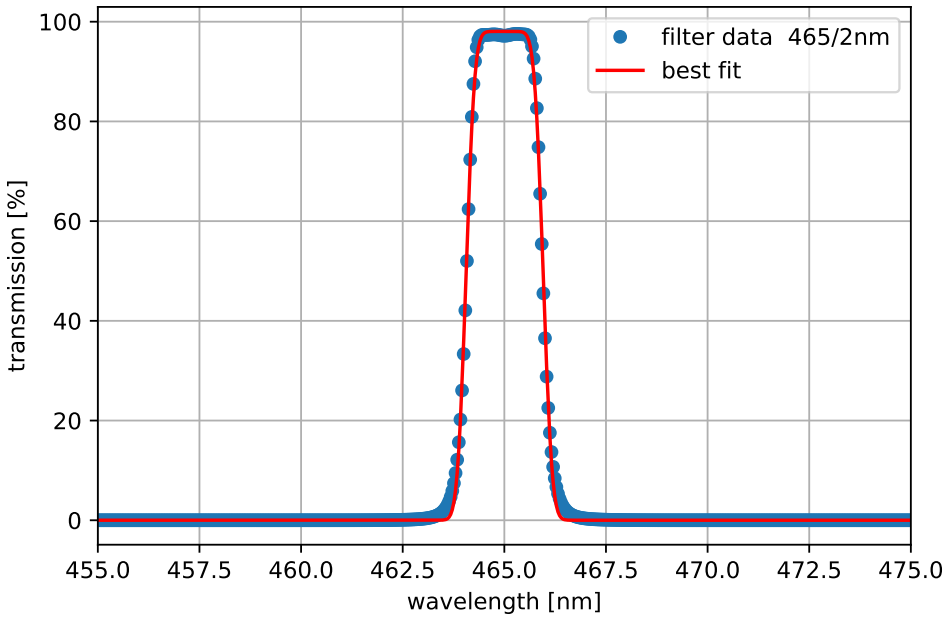

Figure 3.8: Fit of filter data Alluxa [17] with a bandwidth of 2 nm and a central wavelength of 465 nm

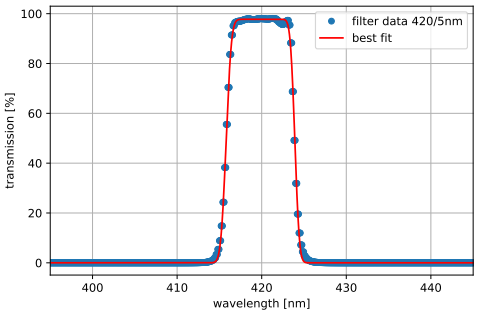

Figure 3.9: Fit of filter data Semrock [20] with a bandwidth of 8.2 nm and a central wavelength of 420 nm

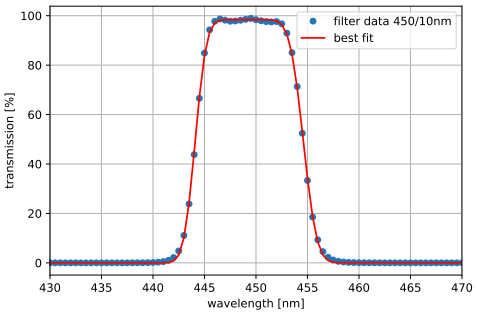

Figure 3.10: Fit of filter data Thorlabs [21] with a bandwidth of 10 nm and a central wavelength of 450 nm

3.1.2 Lenses used in the H.E.S.S. setup

To counter this problem a diverging lens is used to reparallelize the converging rays onto the filter. The used diverging lens has got a focal distance of -7.5cm.

After the rays pass through the first lens and the interference filter, a second lens focuses the rays back together so that the maximal amount of rays hits the PMT. In the initial setup the first lens is put -7.5cm in front of the original focal spot of the H.E.S.S. telescope. The second lens follows after an additional 4 cm distance.

3.2 Ray tracing simulation of H.E.S.S.

The simulation was done with a ray tracing simulation written in Python by Dr. Dmitry Malyshev. The simulation uses the ray data (60,917 rays) obtained by a simulation of the H.E.S.S. telescope in ROot-BAsed Simulator for ray Tracing (ROBAST).ROBAST is a ROOT-based simulation tool which was especially designed for ray tracing simulations with Air Cherenkov telescopes. The ray tracing simulation was extended for this thesis to include some additional features like an offset and a spectral analysis of the rays at the interference filter as well as the possibility to optimize the setup for the measurement time.
Additional code, written in Python and provided by Andreas Zmija, was used to calculate the $g^{(1)}$ and $g^{(2)}$ correlation functions as well as the coherence time.

3.2.1 Light of rays inside the intensity interferometry optics

The ROBAST simulation produces 60917 light rays which are focused on a point 15 m after the mirrors on their light path. Because the diameter of the telescope is 12 m some rays come in with a big angle to the optical axis. The distribution of the angles in the H.E.S.S. telescope can be seen in Figure 3.11. The angles range from about 3.5° to about 27°. Rays with smaller angles are blocked by the shadow of the mount and camera of the telescope which lie on the optical axis (see Figure 3.2).
With these angles the combined spectrum with the 2 nm Alluxa filter is calculated (see Figure 3.12) and compared to the single Alluxa 2 nm filter and an ideal 2 nm rectangle filter function. It can be seen that there is not much difference between the rectangle and the Alluxa filter. The filter is just less steep on the edges. The combined spectrum on the other hand is much broader and also shifted to smaller wavelengths. The reasons for this are discussed in Section 3.1.1.
To get an insight into what that means for the coherence time the normalized frequency spectrum is calculated (see Figure 3.13) by using the Fourier transformation on the wave spectrum. From the normalized frequency spectrum the $g^{(1)}$ correlation function can be calculated via the Wiener-Khintchine theorem (see Section 1.2.1). The $g^{(1)}$ function is then transformed with the Siegert relation (see Section 1.3.1) to get the $g^{(2)}$ function.
The different correlation functions for the different spectra can be seen in Figure 3.14. The coherence time can be defined as the area below the $g^{(2)}$ function and can be calculated by taking the integral. The combined spectrum has got a coherence time of 0.057 ps which is small, compared to the Alluxa filter (0.329 ps) and the ideal bandpass filter (0.352 ps).

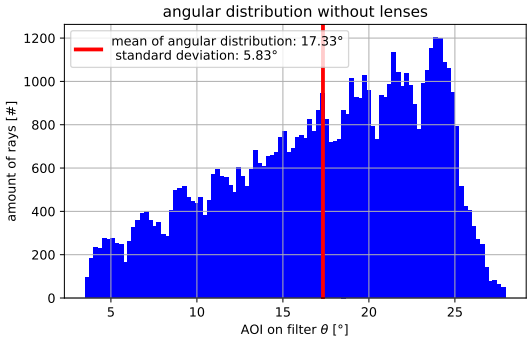

Figure 3.11: Angular distribution of rays that were focused with the H.E.S.S. telescope without additional lenses to further parallelize the light onto the interference filter

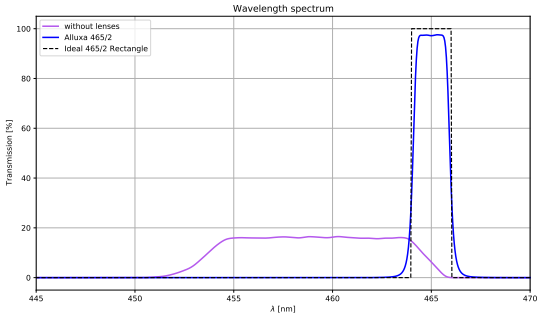

Figure 3.12: Combined spectrum of H.E.S.S. with non parallelized light compared to the spectrum of the Alluxa 2 nm filter and a perfect rectangle spectrum with 2 nm width and central wavelength of 465 nm

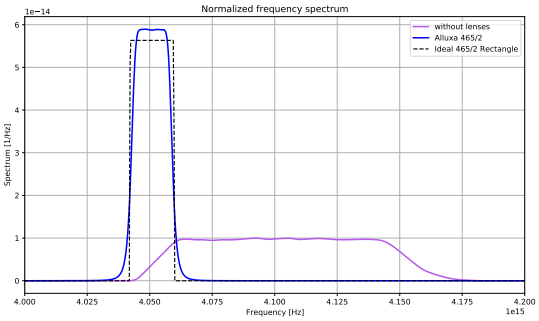

Figure 3.13: Normalized frequency spectrum of the combined spectrum of H.E.S.S. rays without lenses compared to the Alluxa filter spectrum and a perfect rectangle spectrum

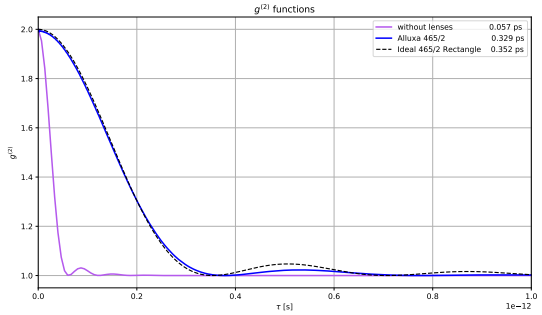

Figure 3.14: $g^{(2)}$ correlation function of the combined H.E.S.S. spectrum compared to the correlation function of the Alluxa filter and a perfect rectangle spectrum as well as their coherence time

This result implies that another setup is needed where the spectrum is not stretched and shifted that much. Because of the short coherence time the signal to noise ratio is so bad that it is hard to even detect a signal.
This improvement can be done by reducing the spread and size of the AOIs on the interference filter. Hence a lens system which parallelizes the rays has to be implemented.
The initial lens setup consists out of two lenses. The first lens with a negative focal length of -7.5 cm, to align the rays with the optical axis so the AOIs get small on the filter, is located exactly -7.5 cm in front of the actual focal spot of H.E.S.S.. The second lens with a positive focal length is 4 cm behind the first one and is used to focus the beams onto the PMT. The light propagation through the setup can be seen in Figure 3.15. The position of the filter between the lenses does not change the produced combined spectrum and in reality the depiction of lenses and filter as purely two dimensional objects is not correct. In the real setup the position of the filter is therefore fixed. On the left the incoming focused rays of H.E.S.S. can be seen. After passing the first lens they become approximately parallel before being focused onto the PMT in the back of the setup by the second lens. But on the way of this propagation some rays hit the outer parts of the 2 inch optics. These rays do not get detected by the PMT. The fraction of surviving rays is another crucial factor in the quality of the detected spectrum. To get an inside how the surviving rays are distributed the ray distribution at the PMT is plotted (see Figure 3.16). The incoming rays all hit the PMT after they passed the lens system. The fraction of surviving rays however is 53%. So nearly half of the rays hit the lens tube and do not contribute to the signal by the PMT. This reduces the incoming photon rate, which enters the necessary measurement time inverse quadratically. It is therefore desirable to increase the transmission fraction. One solution is to move the whole optical system backwards, but then the first lens does not parallelize the rays well anymore. This worsens the shape of the combined spectrum. There is an optimal point in shift to the original setup and the original focal point of the system where these two influences contribute to a best result.

3.2.2 Different shift for the setup

This optimal point can be found by comparing the fraction of surviving rays as well as their spectra. A positive shift means the setup is moved backwards compared to the first setup. Which means a lens system with 1 cm shift is now 6.5 cm in front of the focal point of the H.E.S.S. telescope compared to the original -7.5 cm (see Figure 3.17).
The simulation was done for varying shifts in the range of -1 cm to +3 cm. Figures 3.18, 3.20 and 3.22 show that with increasing shift less rays get blocked by the limited size of the lens tube, but the rays in the central part of the intensity interferometry setup are not parallel anymore. Additional to that not all rays hit the PMT at the end of the setup, because the converging lens does not produce the focal spot at the PMT anymore, but beforehand because of non perpendicular rays. That effect gets worse for bigger shifts, which also is shown in the ray distribution at the PMT (see Figures 3.19,3.21 and 3.23). For small shifts the ray

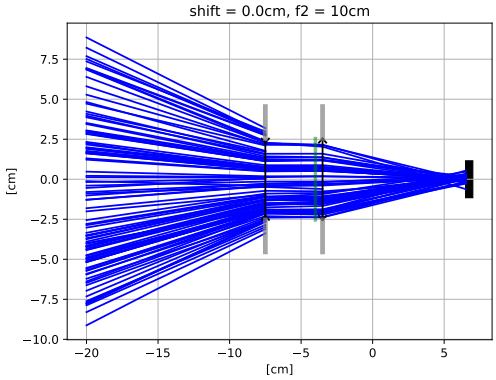

Figure 3.15: Propagation of light rays in the H.E.S.S. interferometry setup with inital conditions. Shift describes the shift of the setup to the H.E.S.S. focal point. f2 is the focal length of the converging lens.

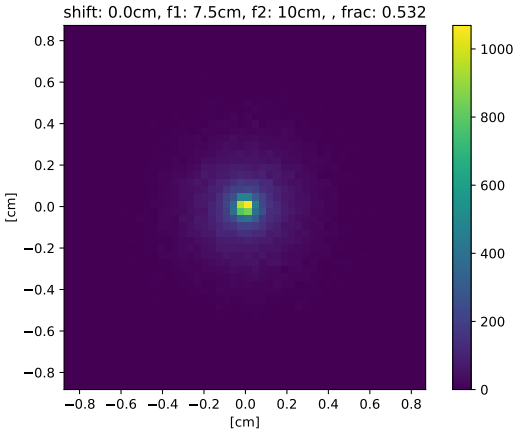

Figure 3.16: Ray distribution at the PMT of the H.E.S.S. initial setup. -f1 is the focal length of the diverging lens. frac describes the fraction of surviving rays of the used setup.

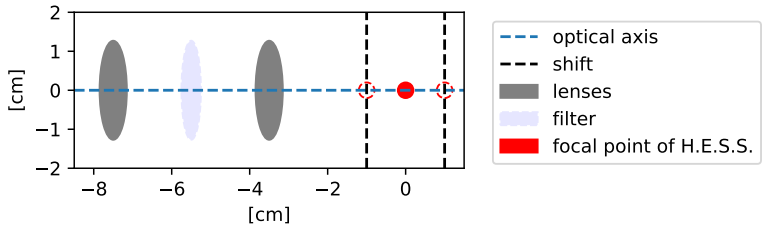

Figure 3.17: The sketch shows how shift effects the focal point if the setup is at a fixed position.

distribution at the PMT is significantly smaller than the PMT. Whereas for 3 cm shift the ray distribution at the PMT gets bigger than the PMT which leads to a smaller fraction of surviving rays.

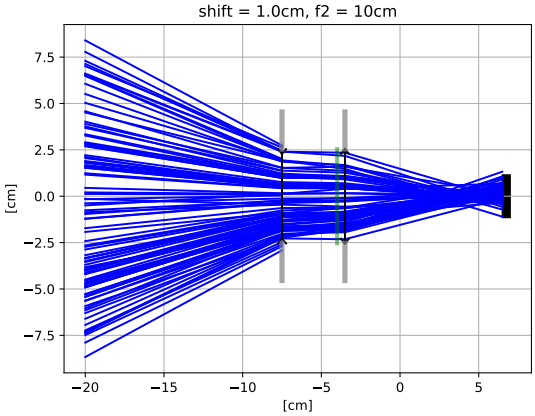

Figure 3.18: Ray propagation for a setup with a shift of +1 cm to the original setup

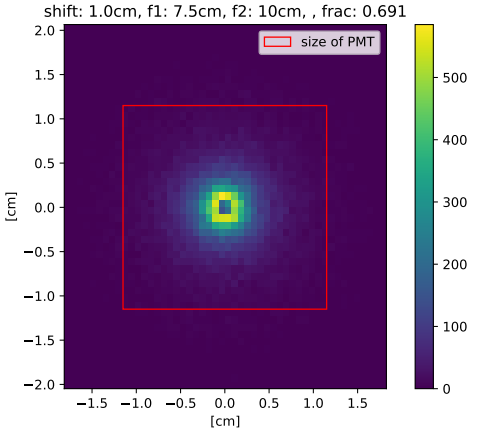

Figure 3.19: Ray distribution at the PMT for a setup with +1 cm shift to the inital setup

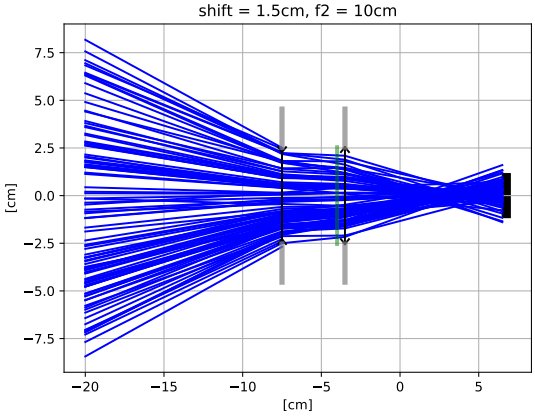

Figure 3.20: Ray propagation for a setup with a shift of +1.5 cm to the original setup

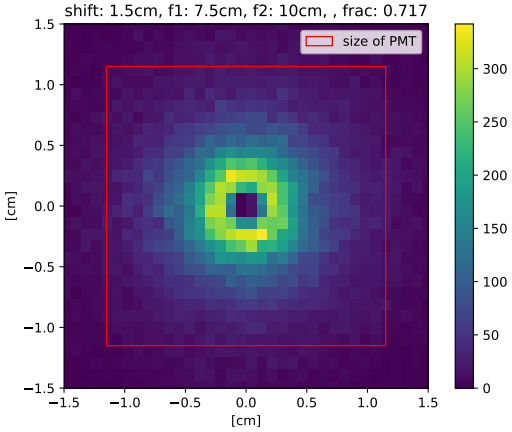

Figure 3.21: Ray distribution at the PMT for a setup with +1.5 cm shift to the inital setup

The course of the fraction is depicted in Figure 3.24. For 1.5 cm shift the fraction reaches its maximum with a 72% survival rate.
But only a good fraction does not make a preferable setup. It also depends on the shape of the filter spectrum which in itself depends on the AOI on the filter. The AOIs on the other hand depend on the applied shift.
The angular distribution of the inital setup ranges from around 0° to roughly 4° (see Figure 3.25). With increasing shift the spread of angles as well as the central wavelength increase (see Figures 3.26, 3.27 and 3.28). The lack of rays with no AOI for higher shift is explained by the shadow of the camera and the mount in the direct path of the line of sight.
The mean and standard deviation of the angular distribution provides a good impression of how the rays behave at the interference filter (see Figure 3.29).

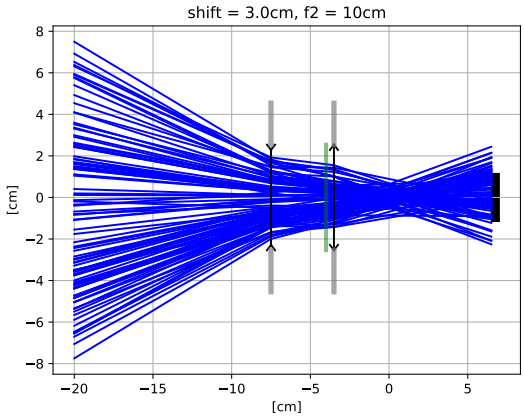

Figure 3.22: Ray propagation for a setup with a shift of +3 cm to the original setup

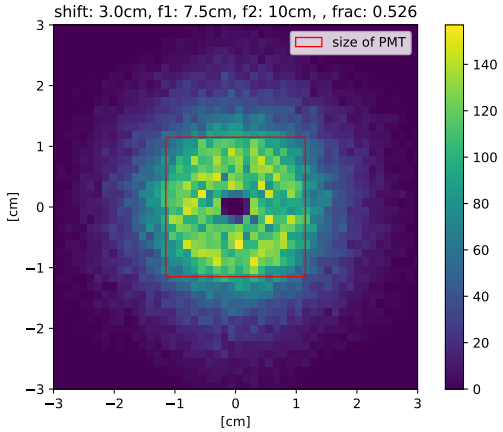

Figure 3.23: Ray distribution at the PMT for a setup with +3 cm shift to the inital setup

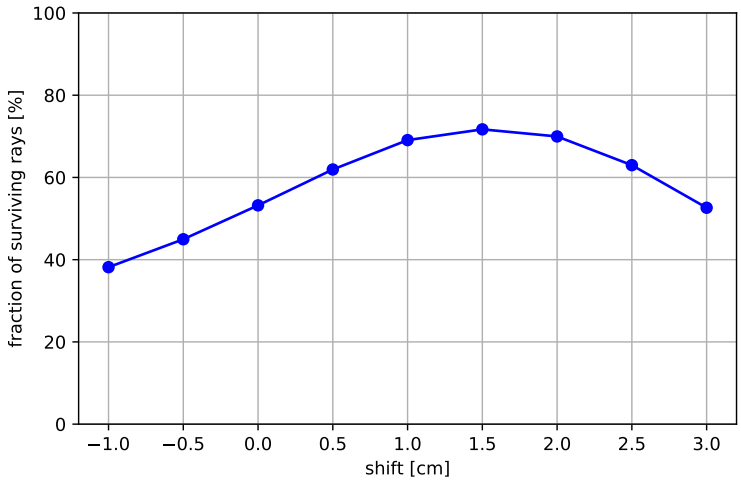

Figure 3.24: Trend of fraction of surviving rays dependent on the set shift

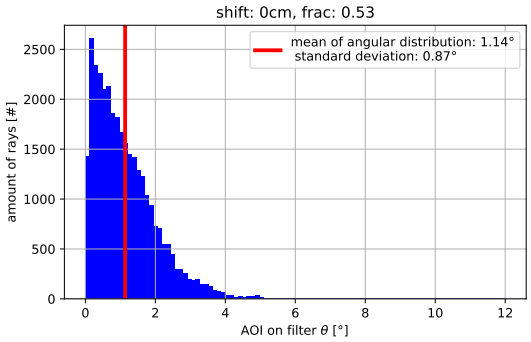

Figure 3.25: Angular distribution of the light rays at the interference filter with no shift

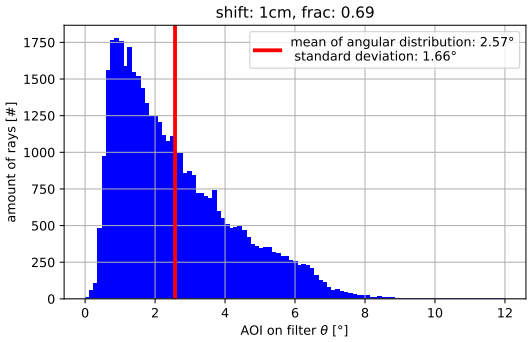

Figure 3.26: Angular distribution of the light rays at the interference filter with 1 cm shift

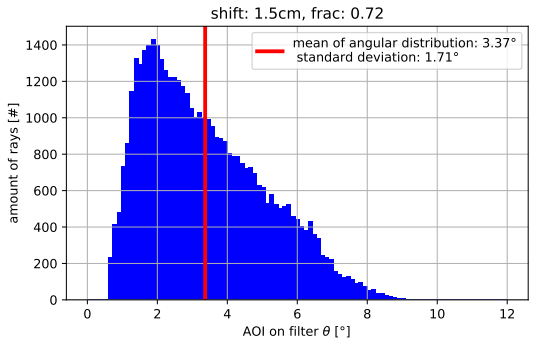

Figure 3.27: Angular distribution of the light rays at the interference filter with 1.5 cm shift

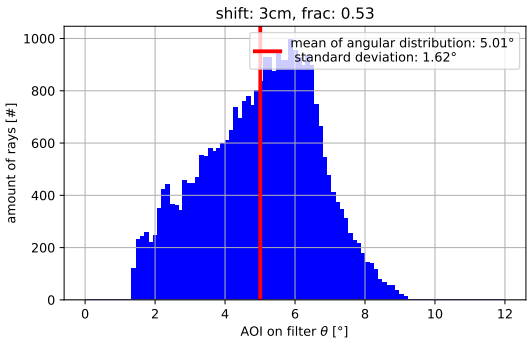

Figure 3.28: Angular distribution of the light rays at the interference filter with 3 cm shift

The mean angle of the distribution increases with increasing shifts. The minimum is at -0.5 cm with around 1° while the maximum is at 3 cm shift with 5°. The standard deviation is shaped similar up to 1 cm after that it stays roughly constant at around 1.7°. This means the distribution does not increase in width after 1 cm and only shifts to bigger mean angles.

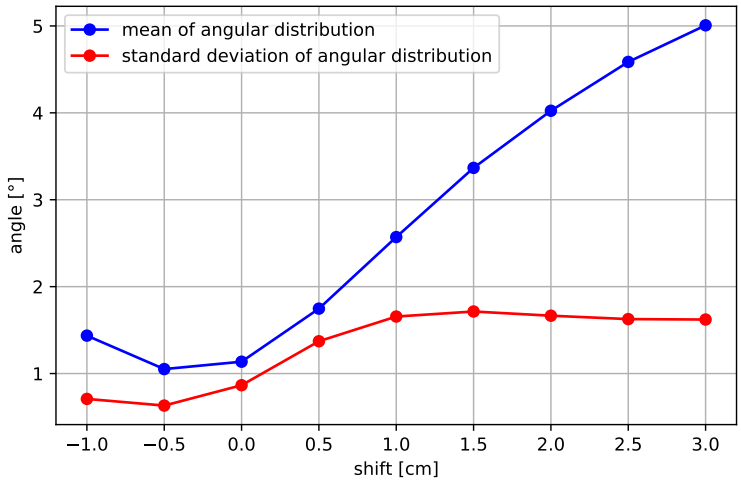

Figure 3.29: Mean and standard deviation of the angular distribution for different shifts

The fitfunction of the filter data (see Figure 3.8, 3.9 and 3.10) is shifted for every angle in the angular distribution and added to a combined spectrum. After that the spectrum gets normalized by the amount of rays that entered the setup in the beginning. This procedure is done for every filter and simulated shift. This means the transmission is not the transmission function of the filter, but of all rays in the setup that are detected at the PMT. The resulting spectra can be seen in Figure 3.30, 3.31 and 3.32.
While the spectra for the Semrock and the Thorlabs filter did not change much in central wavelength and width, but only in height due to the different fractions for each shift, the spectrum for the Alluxa filter changes in shape, central wavelength and width. The central wavelength is clearly shifted to higher frequencies while the shape changes from a near rectangular outline to a more Gaussian shaped

function. The transition is calculated by adding the single spectrum of each ray and then dividing by the total amount of initial rays 60,917. This is done so the spectrum reflects the aspect of a non 100% transmission of the initial rays through the system.

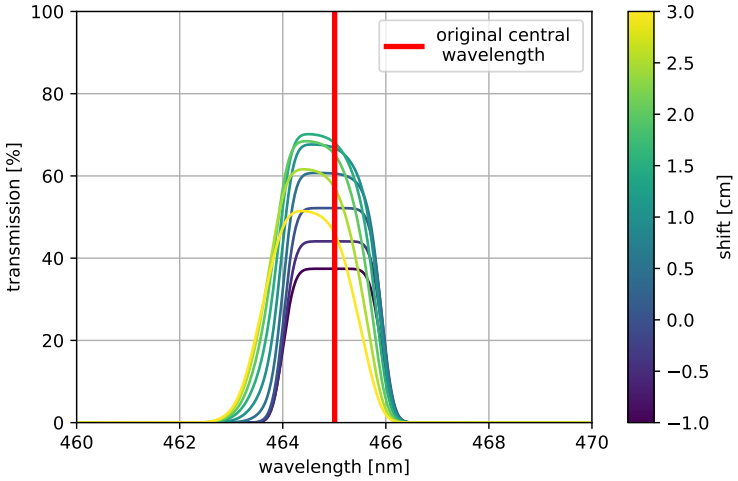

Figure 3.30: Depiction of the different combined spectra for different shift in the setup in respect to the H.E.S.S. focal point while using the Alluxa 2 nm interference filter

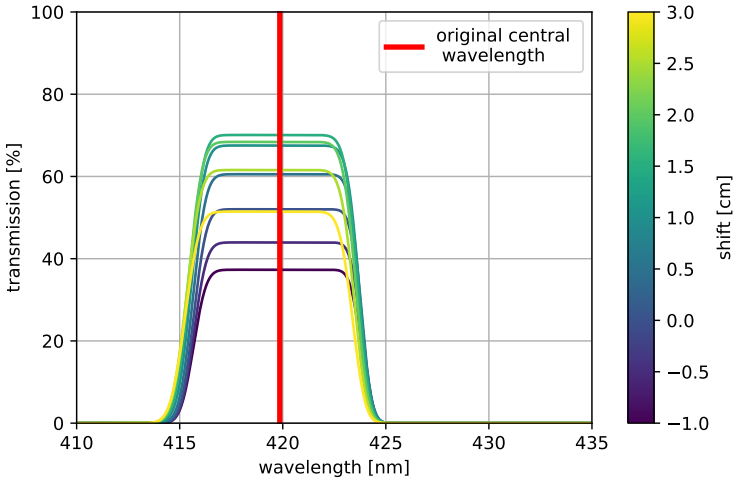

Figure 3.31: Depiction of the different combined spectra for different shift in the setup in respect to the H.E.S.S. focal point while using the Semrock 8.2 nm interference filter

For a decision which filter and which shift poses an optimum for the planned measurement, a quantitative measure of the quality of the spectrum is needed which factors in the fraction of surviving rays as well as the shape and width of the combined spectrum. A quantity that expresses the quality of the spectrum is the required measurement time T for any significance n:

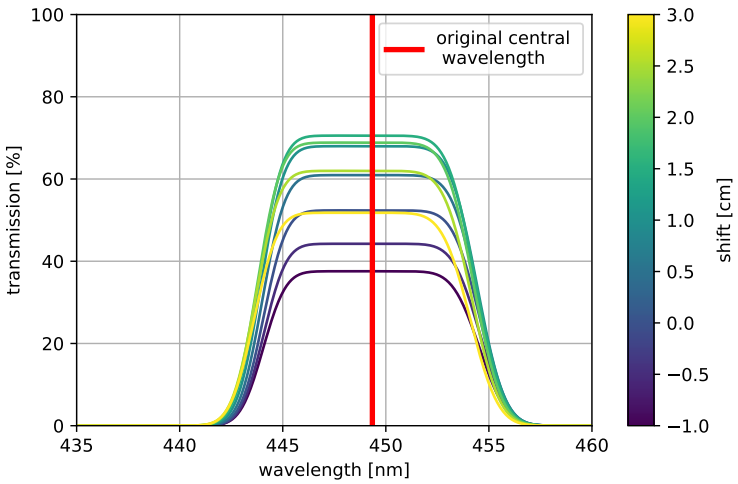

Figure 3.32: Depiction of the different combined spectra for different shift in the setup in respect to the H.E.S.S. focal point while using the Thorlabs 10 nm interference filter

$$T = \frac{4n^2\sigma_t c^2(\Delta\lambda)^2}{k^2\lambda_0^4 \dot{N}_0 \dot{N}_1}[22] \tag{3.4}$$

with

- k being a factor taking the filter function into account e.g. k=1 for Lorentzian and k = 0.667 for Gaussian light
- λ_0 the central wavelength
- $\Delta\lambda$ the optical bandwidth
- σ_t the time resolution of the system
- $\dot{N}_i$ the photon rate at photo detector i since the setup later will use a beamsplitter with two PMTs in its arms.

For a comparison of the different simulations an absolute value for T is not necessary and depends on the final choice of required significance. The following proportionality is used:

$$T \propto \frac{\mathrm{FWHM}^2}{\lambda_0^4 \cdot \int_{\mathrm{spectrum}}} \tag{3.5}$$

with λ_0 being the central wavelength. Full width half maximum (FWHM) is used to describe $\Delta\lambda$ the optical bandwidth. As a measure of the photon rate the integral over the spectrum is used. Because of the normalization of the spectrum this combines the information of the fraction via the height of the spectrum as well as the relative photon rate produced by each filter which gives to account that because of the different bandwidths the filters also have different related photon rates.

The optimal setup is determined by calculating the measurement time and then fitting it to find the minimum. This was done for the Alluxa filter (see Figure 3.33 and the setup with no lenses (see Figure 3.34) as well as the Semrock filter 3.35 and the Thorlabs filter (see Figure 3.36). Each curve is normalized to the minimum. These plots show that the optimal shift seems to be independent of the used filter 1.5 cm. The comparison between the setup with lenses to the one without lenses is a good indication that the lenses are necessary for improving the measurement. The measurement time is about 20.4 times bigger than the one with 1.5 cm shift. The shift of 1.5 cm shows an improvement of about a factor 1.5 to the original setup. The data show quadratic behavior.

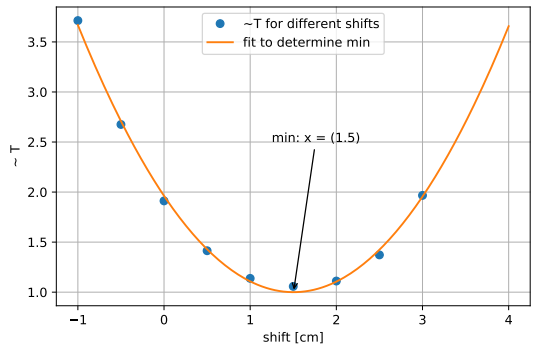

Figure 3.33: Measurement time over shift for 2 nm filter

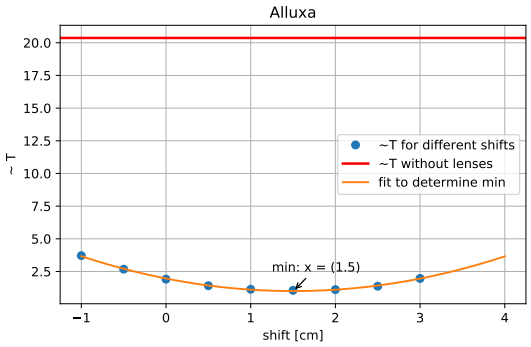

Figure 3.34: Comparison Alluxa with and without lenses

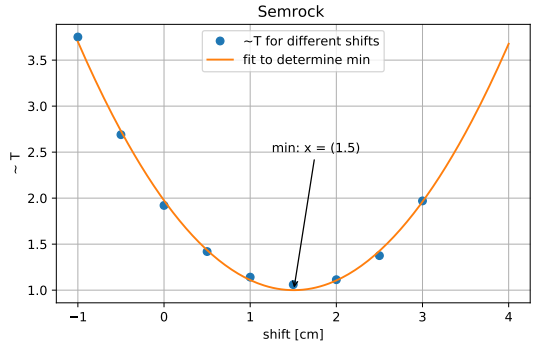

Figure 3.35: Measurement time over shift for 8.2 nm filter

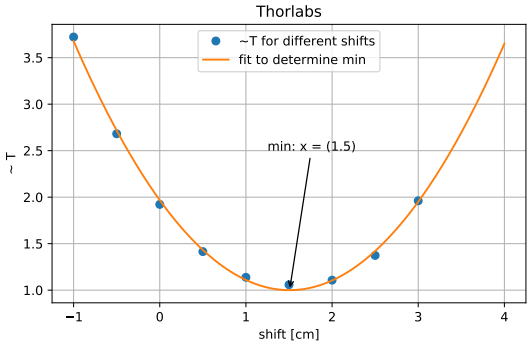

Figure 3.36: Measurement time over shift for 10 nm filter

Because the data are normalized they can not be compared directly. For that reason the data from the Alluxa filter with 1.5 cm shift were taken and used to again normalize the data from the other two filters. The comparison in Figure 3.38 shows that the measurement with the Alluxa filter produces significant data with a factor of 1.52 respectively 1.15 times quicker than with the other filters. The optimal spectra are shown in Figure 3.37.

The optimal spectra for the different filters are depicted in Figure 3.37 and their respective $g^{(2)}$ in Figure 3.39. τ_c of the optimal shift Alluxa spectrum with 0.312 ps is significantly longer than τ_c of the Semrock filter 0.067 ps or the Thorlabs 0.056 ps.

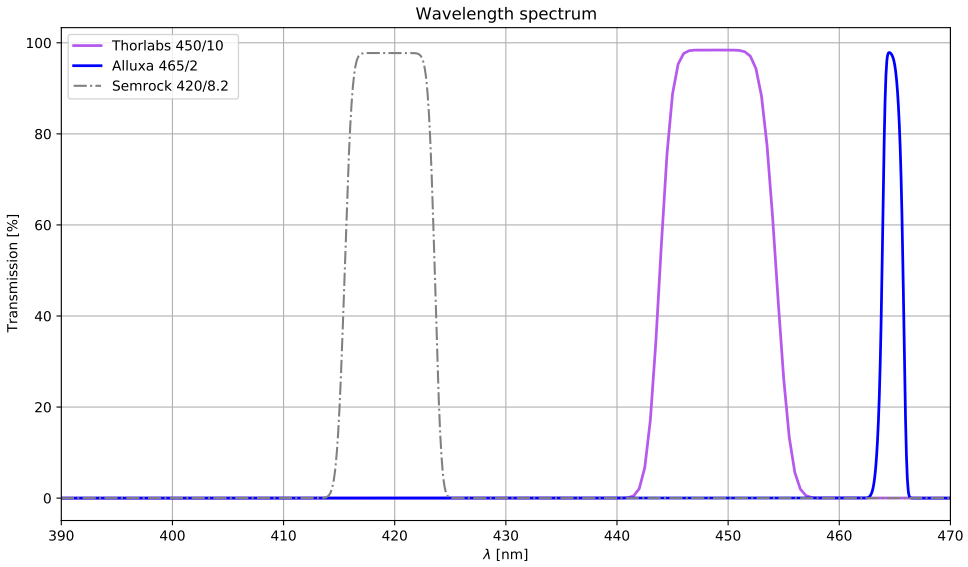

Figure 3.37: Comparison of the combined spectra of the different interference filters

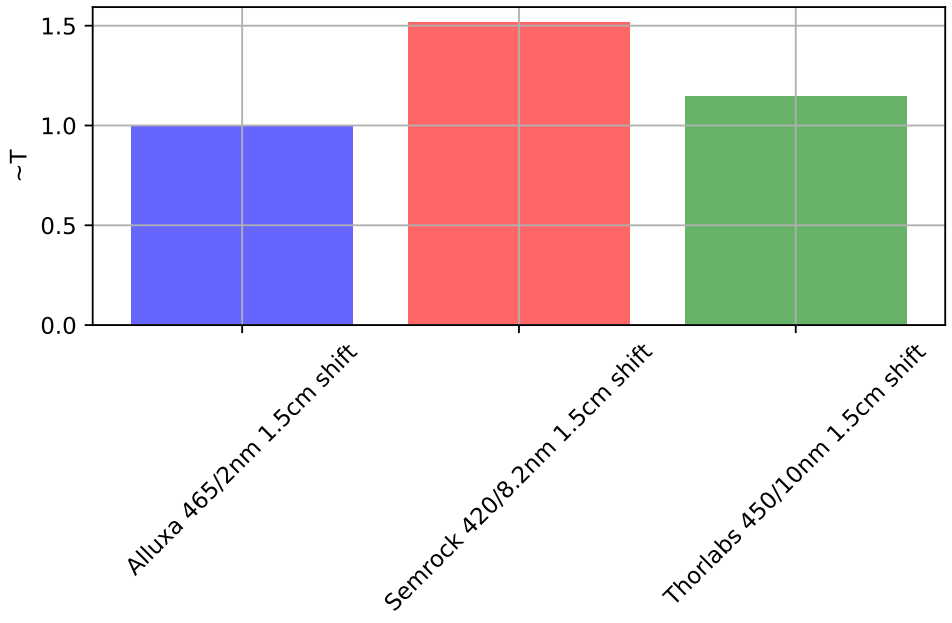

Figure 3.38: Comparison of the measurement time for the optimal setup with different filters

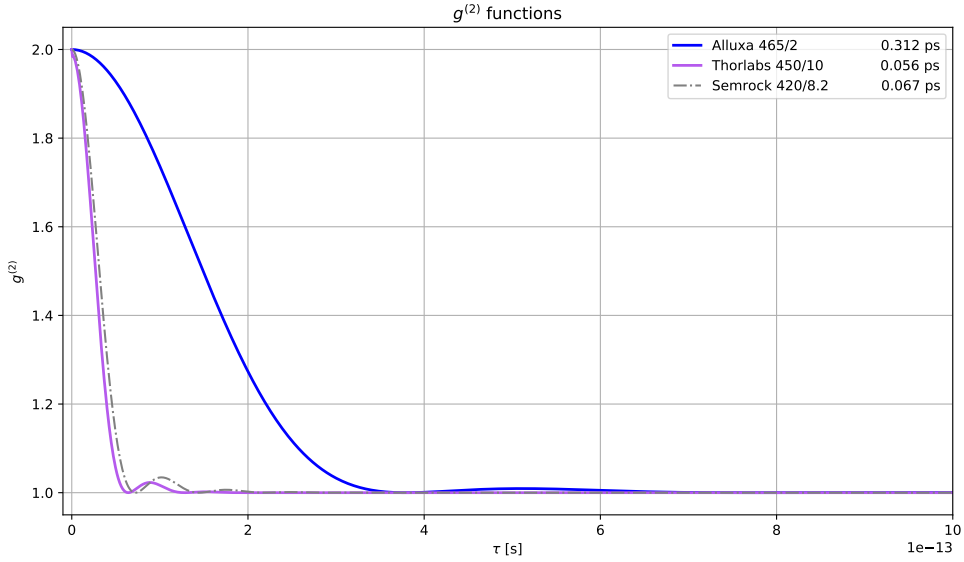

Figure 3.39: Correlation function $g^{(2)}$ for different filters with the optimal shift of 1.5 cm

A complete list of the coherence times is shown in Table 3.1. It shows that the Alluxa filter also has a superior coherence time and that the optimal combined spectrum does not loose a lot coherence compared to the single Alluxa coherence time.

filter	shift	coherence time
Alluxa 2 nm single spectrum	-	0.329 ps
perfect 2 nm rectangle	-	0.352 ps
Alluxa 2 nm H.E.S.S. without lenses	-	0.057 ps
Alluxa 2 nm H.E.S.S. combined spectrum	1.5 cm	0.312 ps
Semrock 8.2nm H.E.S.S. combined spectrum	1.5 cm	0.067 ps
Thorlabs 10nm H.E.S.S. combined spectrum	1.5 cm	0.056 ps

Table 3.1: Comparison of the coherence time of different setups

All this together leads to the conclusion that using the Alluxa filter with a shift of 1.5 cm is beneficial for the measurment time as well as the coherence time. But to get to a final conclusion on the optimal setup, further investigations need to be done.

3.2.3 Focal length diverging lens

The setup consists out of two lenses. The first lens is necessary for parallelization of the rays. If the setup is shifted closer to the focal point of the telescope the parallelization needs to be done in a shorter distance. This suggests to test out a lens with shorter focal distances. The chosen focal length for tests is -6 cm. This value was chosen because in theory it should compensate for the 1.5 cm shift. The propagation in Figure 3.40 shows the propagation of rays with the shorter focal length. The first lens with focal length -6 cm is placed -7.5 cm before the actual

focal spot of H.E.S.S.. Which means the focal spot of H.E.S.S. and the lens are not in alignment anymore for the case of zero shift. The ray distribution at the PMT for these settings (see Figure 3.41) looks similar to the one with the -7.5 cm focal length and -1 cm shift (compare to Figure 2). Which is not surprising since the -6 cm focal length lens is 1.5 cm before the point where the focal points of lens and H.E.S.S. align.

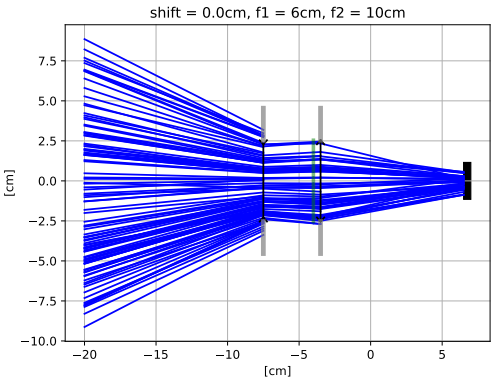

Figure 3.40: Ray trace picture of the setup with no shift in respect to the initial setup and a lens with a -6 cm focal length

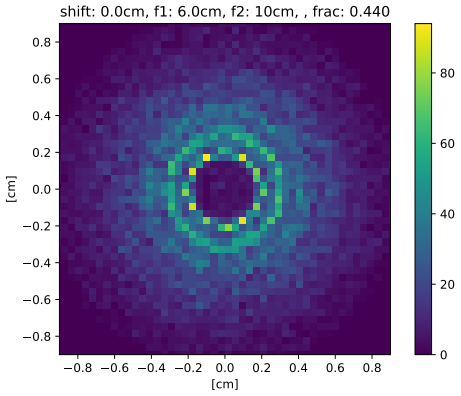

Figure 3.41: Ray distribution at the PMT of setup with a -6 cm lens and no shift

This is why the whole setup needs to be shifted as well. Two examples for that are Figure 3.42 and Figure 3.44 with 2.2 cm and 4 cm shift respectively. Compared to the same setup without shift more rays are able to pass the first lens for both shifts. For 4 cm shift the waist of the beam is clearly unnecessary small. The non-uniformity of incoming angles of rays in this case leads to the inability of second lens to focus the rays onto the PMT sufficiently because some rays are refracted so much that they miss the PMT entirely. This also shows if both ray distributions are compared (see Figures 3.43 and 3.45) to each other. For 2.2 cm shift the majority of rays is contained inside detecting area while for 4 cm shift a non-negligible share of rays is leaking out of this area.
The combination of the factors leads to a distribution of the fraction of surviving rays dependent on the shift (see Figure 3.46). In comparison to the previous simulation the maximum of fraction is shifted to bigger values. This is the case, because the loss at the first lens is minimized while simultaneous making sure the rays stay in bound. For small shifts the simulation predicts smaller fraction compared to the previous result, but with increasing shift the fraction of the -6 cm simulation overtakes the one with -7.5 cm. This happens for a shift of 1.5 cm, where the simulation with the -7.5 cm lens has its maximum. The maximal fraction for the -6 cm lens occurs for a shift of 2.2 cm. The transmitted fraction of rays is around 12.8% greater for the lens with smaller focal length of -6 cm.
Figure 3.47 shows the angular distribution on the interference filter of three selected setups: Two distributions are produced while using the -6 cm lens with 1.5 cm and 2.2 cm shift. The remaining distribution is created while using the -7.5 cm lens with 1.5 cm shift. It becomes apparent that the reason for inserting the -6 cm lens is valid. More rays have an AOI around 0° compared to the simulation

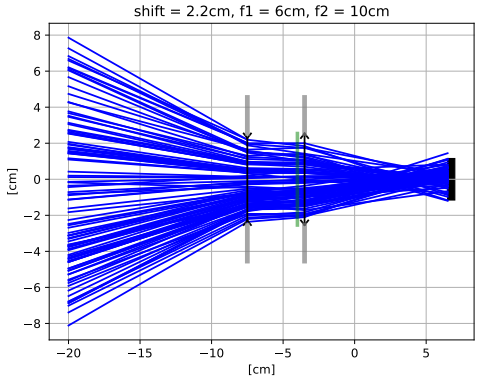

Figure 3.42: Ray trace picture of the setup with 2.2 cm shift in respect to the initial setup and a lens with a -6 cm focal length

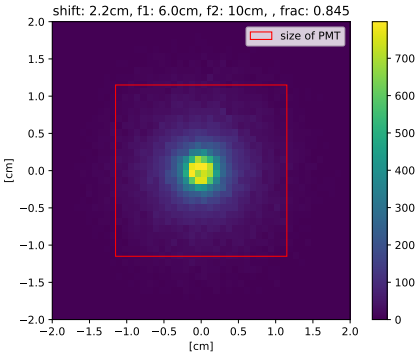

Figure 3.43: Ray distribution at the PMT of setup with a -6 cm lens and 2.2 cm shift

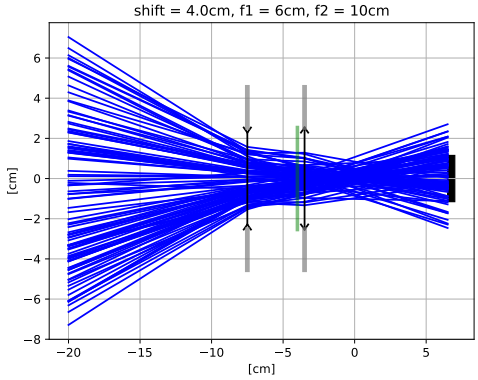

Figure 3.44: Ray trace picture of the setup with 4 cm shift in respect to the initial setup and a lens with a -6 cm focal length

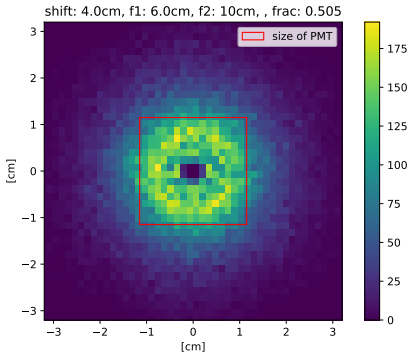

Figure 3.45: Ray distribution at the PMT of setup with a -6 cm lens and 4 cm shift

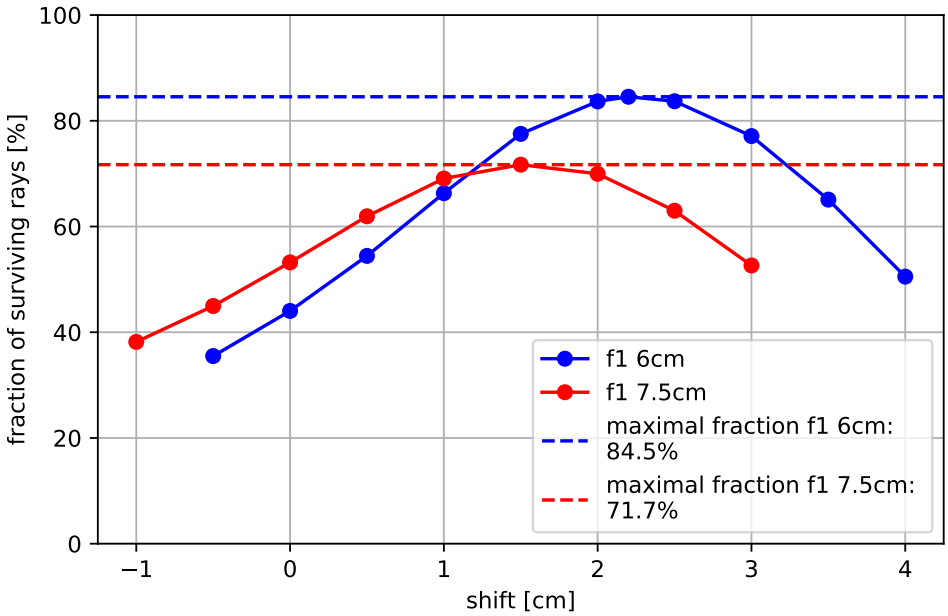

Figure 3.46: Comparison of fraction of surviving rays for different focal length of the diverging lens f1

with the -7.5 cm lens. This means the light gets parallelized more effectively. Together with the bigger fraction the measurement time should be smaller for this lens. The comparison of the two -6 cm distributions shows that for 1.5 cm shift the rays have smaller angles. This is not surprising since with 1.5 cm shift the lens' focal spot aligns perfectly with the one from H.E.S.S..

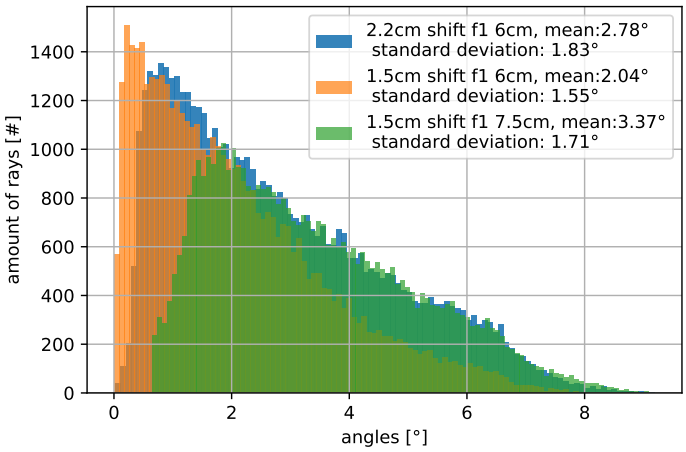

Figure 3.47: Angular distributions of different focal lengths and shifts

The mean of the angular distribution (see Figure 3.48) looks quite similar to the one with the -7.5 cm lens (see Figure 3.29), just shifted around 1.5 cm. The same applies for the standard deviation with the exception of a small decrease starting

at 3 cm shift. This difference of 1.5 cm can be explained by the change of focal distance of 1.5 cm from 7.5 cm to 6 cm.

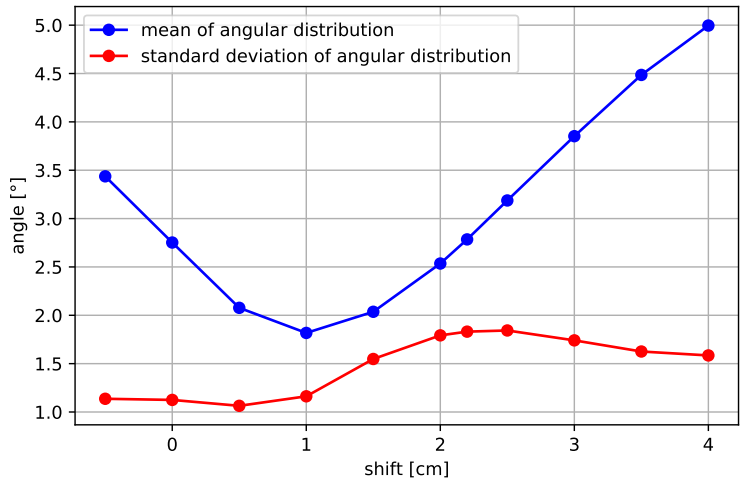

Figure 3.48: Course of the mean value and standard deviation with the -6 cm lens for varying shifts

The spectra produced from the angular distributions (see Figure 3.49), similar to the one for the other focal length (see Figure 3.30), starts with a small transition percentage and rectangle shape with flatter slope on the edges to a spectrum which is more Gaussian shaped and has its maximum for 2.2 cm shift. For increasing shifts the central wavelength is shifted to smaller wavelengths increasingly.

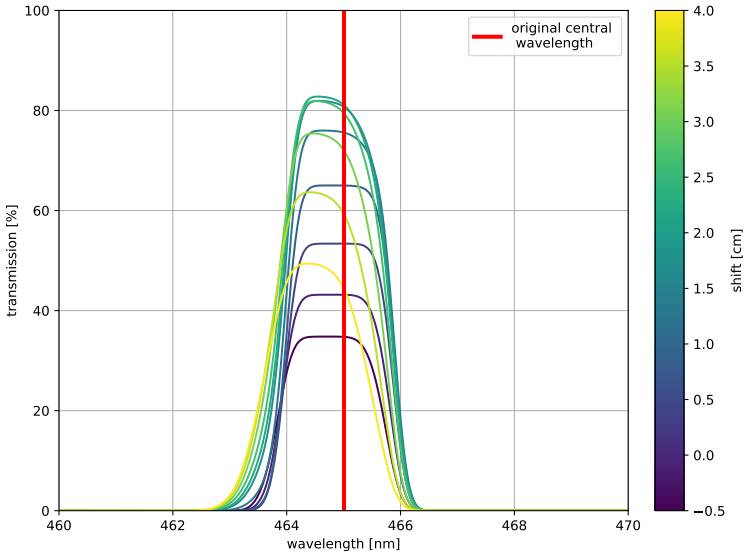

Figure 3.49: Influence of shift on the spectra produced by the setup using the -6 cm lens

For quality comparison of the setups Equation 3.5 is again used to calculate a value which is proportional to the measurement time. Figure 3.50 shows the measurement time of both lenses with different shifts. For small and negative shifts the lens with bigger focal length proves to be advantageous, but beginning

with 1.5 cm shift the advantage flips and the -6 cm lens seems to be superior. The minimum for the -6 cm lens is 1.39 times smaller than the one for the -7.5 cm lens. For both lenses the fraction of surviving rays seems to be the dominant factor in determining T.

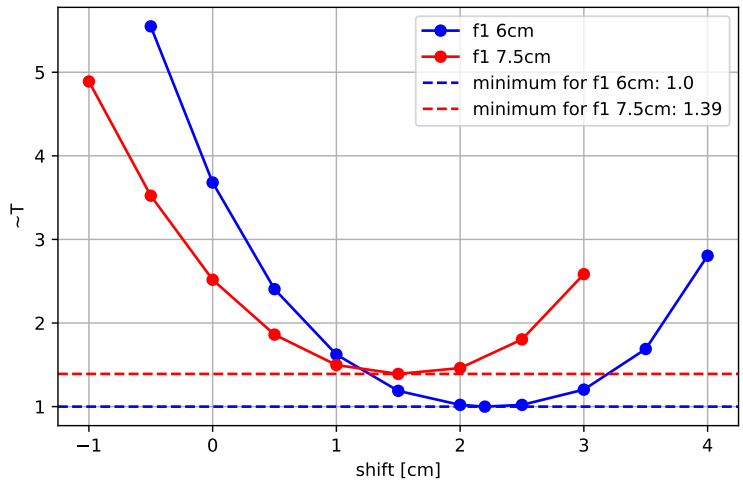

Figure 3.50: Comparison of the measurement time curves for both diverging lenses

3.2.4 Stability of setup to inaccurate pointing

Another aspect that has to be taken into account for a good setup is inaccurate pointing of the telescope. The H.E.S.S. telescopes are constructed to detect Cherenkov air showers which are created in the atmosphere and they are not optimized for tracking a point-like light source such as stars with very high precision. One additional factor for inaccurate pointing is that some stars which are observation targets have low elevation and the heavy camera bend the mount due to gravity in such a way that the CCD camera in the telescope dish (see Figure 3.2), which is used for orientating the telescope in the right direction, aims at the correct source but the mount as well as the interferometry setup do not. These cases of inaccurate pointing should be examined further.

If the telescope's view varies just slightly from the intended one, the light from the observed star gets reflected by the mirror of the interferometry setup in an incorrect way. In the simulation this error is realized by focusing the star light with an offset onto the interferometry setup. The offset was implemented with positive values, meaning the telescope has to little elevation as well as with negative values, meaning the telescope has to much elevation (see Figure 3.51).
The examination of the effect the offset has on the spectrum and the measurement time was done for both -6 cm (see Figures 3.52 and 3.53) as well as -7.5 cm (see Figures 3.54 and 3.55) for the focal length of the diverging lens. The offset is depicted for both a moderate positive and for a negative value of 0.5 cm respectively -0.5 cm. For both different setups the bunch of rays coming out of the telescope is moved in the same way because the lens is placed in the same spot (difference in

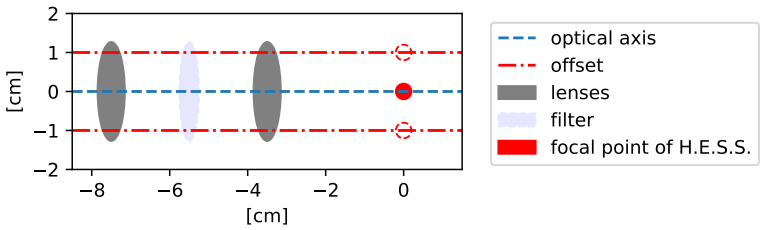

Figure 3.51: The sketch shows how offset effects the focal point if the setup is at a fixed position.

depiction comes from random selection of rays to plot). The offset only shows on the edges of the lens where there is a small bias in the opposite direction of the offset which rays are transmitted further into the setup.
The changes to the setup become more apparent between the two lenses where the interference filter is located. Because of the offset, the rays do not get diffracted at the first lens in the intended way. The general direction of the rays is not parallel to the optical axis or even symmetrical around it, but have a general direction. For a positive offset the rays are on average propagating upwards and the other way around for a negative offset. The second lens amplifies the deviation from the optical axis even further. The result is that a smaller percentage of rays hits the PMT. The rest of the light shines by the detection area.

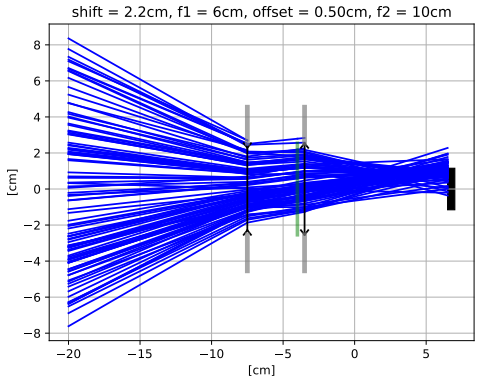

Figure 3.52: Ray trace picture for the setup with 2.2 cm shift a f1 focal length of -6 cm and an offset of 0.5 cm

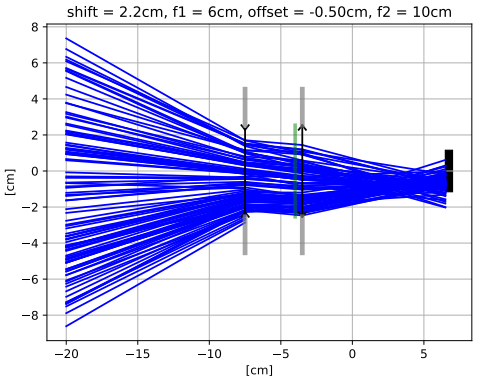

Figure 3.53: Ray trace picture for the setup with 2.2 cm shift a f1 focal length of -6 cm and an offset of -0.5 cm

As the propagation plots suggest the ray distribution at the PMT is shifted from the optical axis according to the offset (see Figures 3.56 and 3.57 for focal length of -6 cm and Figures 3.58 and 3.59 for -7.5 cm). The comparison of the ray distribution at the PMT with Figure 3.21 reveals that the ray distribution at the PMT is not just shifted, but also twisted. For zero offset the ray distribution at the PMT shows equal concentration of rays around the center. If an offset is applied, this is changed and the edge in direction of the offset has a greater intensity than the opposite side. Between the last lens and the PMT the rays coming from below the optical axis end up above it and the other way around because they are behind their focal point. If the offset cuts off a part of the bunch

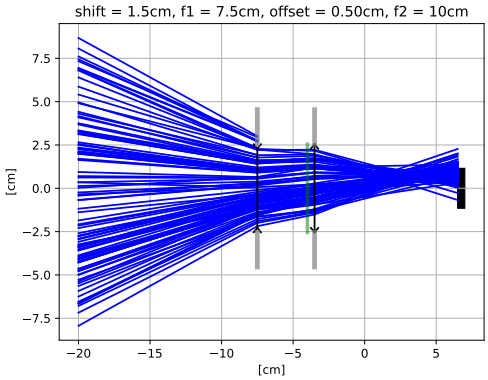

Figure 3.54: Ray trace picture for the setup with 1.5 cm shift a f1 focal length of -7.5 cm and an offset of 0.5 cm

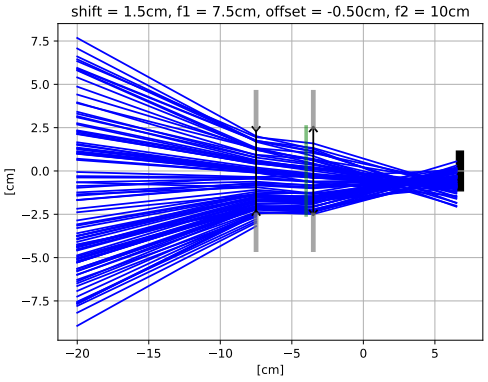

Figure 3.55: Ray trace picture for the setup with 1.5 cm shift a f1 focal length of -7.5 cm and an offset of -0.5 cm

on one side the relative intensity decreases in this area. Because the rays are twisted the largest concentration of rays end up closer to the edge of the detection area.

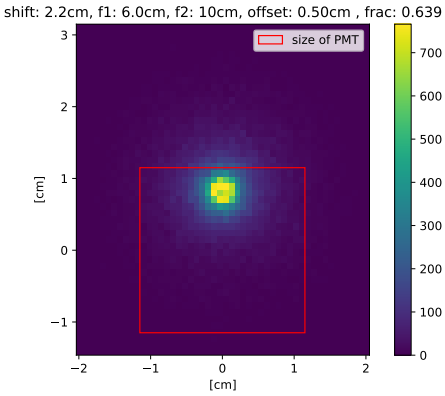

Figure 3.56: Ray distribution at the PMT of the setup with 2.2 cm shift f1 focal length -6 cm and an offset of 0.5 cm

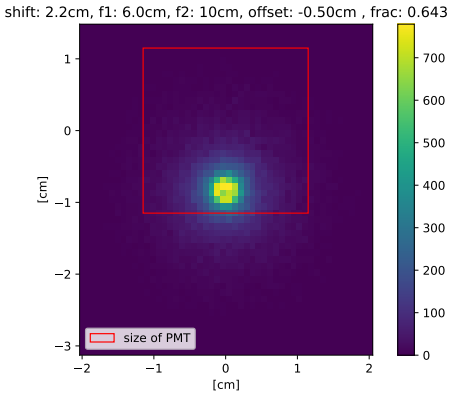

Figure 3.57: Ray distribution at the PMT of the setup with 2.2 cm shift f1 focal length -6 cm and an offset of -0.5 cm

The resulting fractions for both focal lengths are shown in Figures 3.60 and 3.61. For both setups the maxmimum fraction is for zero offset and gets worse for bigger offsets. The stability against small and moderate offsets is largest for moderate shifts like 2.2 cm and 1.5 cm respectively, but for bigger offsets setups with extreme shift proves to be more stable. For ± 1 cm offset moderate shifts drop steeply in fraction with a strong trend, while for both focal lengths the setups with -1 cm and 3 cm shift the fraction does not drop that strongly. The fraction of surviving rays drops under 25% for every setup with an offset ≥ 1 cm.
This occurs for large shifts because the ray distribution at the PMT is quite big and still partially covers the detection area even if its center is outside of it (see Figure 3.62).
For small and negative shifts the fraction does not drop as much, because the initial ray bunch has great width when it encounters the setup. Even for a high

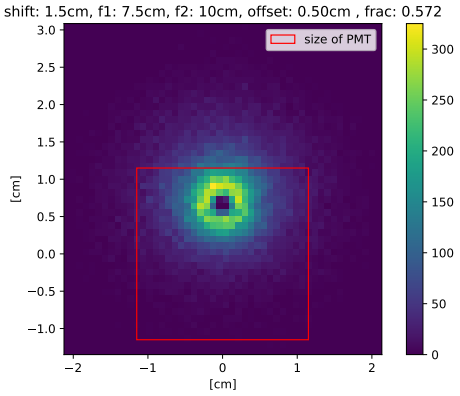

Figure 3.58: Ray distribution at the PMT of the setup with 1.5 cm shift f1 focal length -7.5 cm and an offset of 0.5 cm

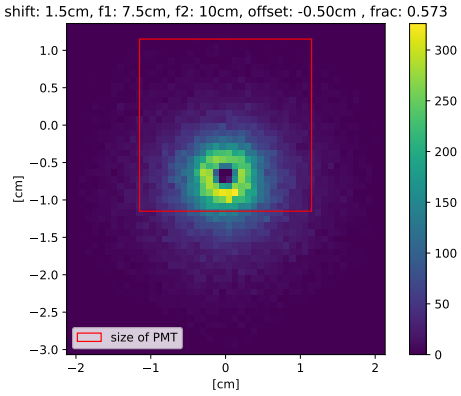

Figure 3.59: Ray distribution at the PMT of the setup with 1.5 cm shift f1 focal length -7.5 cm and an offset of -0.5 cm

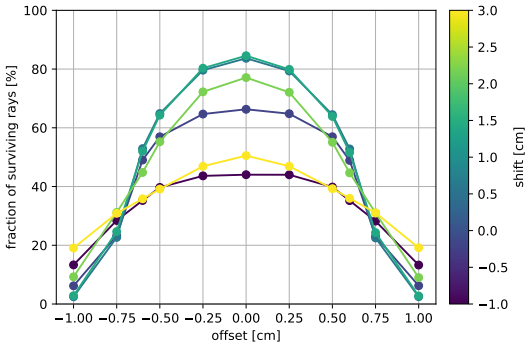

Figure 3.60: Fraction of surviving rays over offset with a f1 focal length of -6 cm

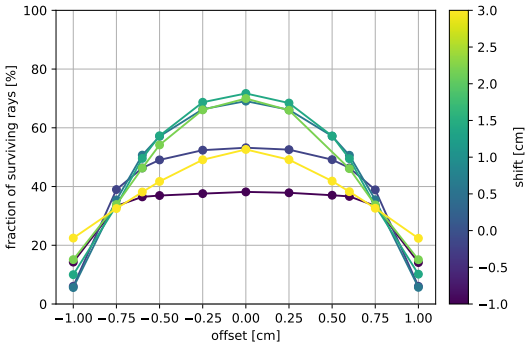

Figure 3.61: Fraction of surviving rays over offset with a f1 focal length of -7.5 cm

offset there are still rays that pass the lens at opposite the side to the offset and reach the PMT (see Figure 3.63).

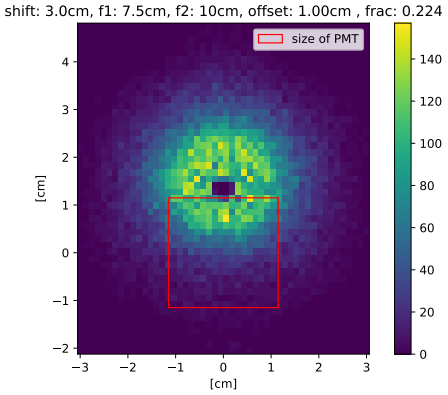

Figure 3.62: Ray distribution at the PMT of a setup with 3 cm shift to demonstrate why it is more stable to offset

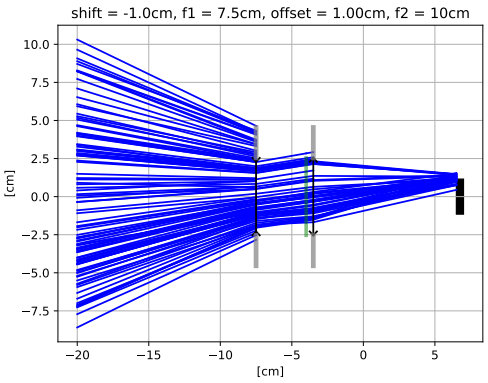

Figure 3.63: Ray trace picture of a setup with -1 cm shift to demonstrate why it is more stable to offset

As indicated by the fraction the angular distribution (see Figure 3.64) confirms that the setup is almost symmetrical to offset. The same is the case for -7.5 cm focal length (see Figure 3.65). In general the mean is smallest for 0 cm offset. The only exception is the setup with 3 cm shift, where the mean is roughly constant with 5°. This is true for both focal lengths. The reason for that is that as the ray distribution at the PMT migrates out of the detection area an increasing percentage of rays at the edge will hit the PMT. These rays are also the rays which happen to have greater AOIs. Because of the size of the ray distribution at the PMT of the 3 cm shift setup being of similar size as the PMT this effect does not occur that strongly if at all.

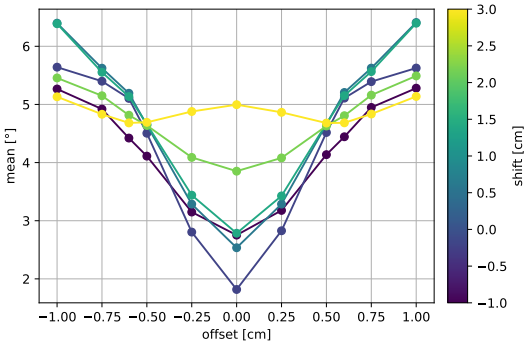

Figure 3.64: Plot of the mean angle of the angular distribution with varying shifts and a f1 focal length of -6 cm

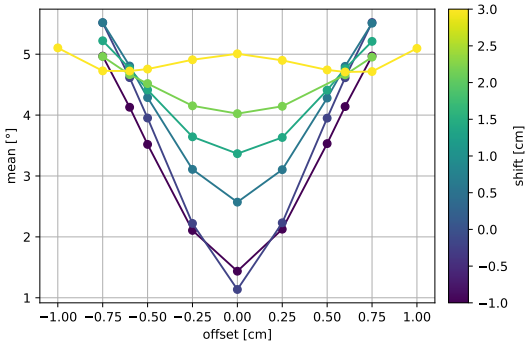

Figure 3.65: Plot of the mean angle of the angular distribution with varying shifts and a f1 focal length of -7.5 cm

The discussed symmetry to offset in the setup can also be seen in the combined spectra (see Figures 3.66 and 3.67). The curves with +offset and -offset are indistinguishable from each other. The increasing shift to smaller wavelengths is caused by the increased AOIs of the rays as well as the steep drop in intensity

become apparent.

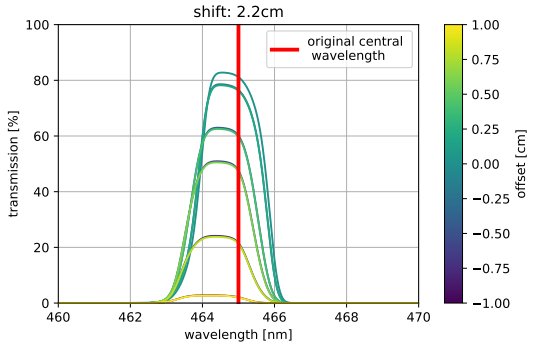

Figure 3.66: Spectra with the optimal shift 2.2 cm and varying offsets for a focal length of -6 cm

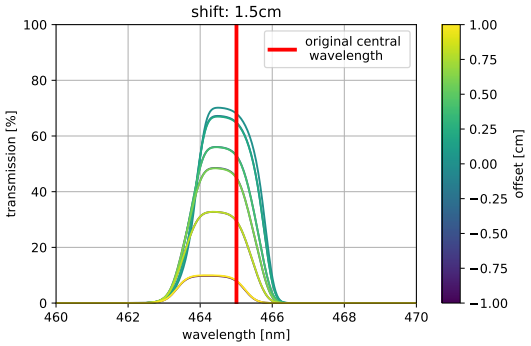

Figure 3.67: Spectra with the optimal shift 1.5 cm and varying offsets for a focal length of -7.5 cm

The shift of the central wavelength, but especially the big drop in fraction have a large impact on the measurement time seen in Figures 3.68 and 3.69. While small offsets up to around ±0.5 cm do not increase the measurement time significantly, the increase for larger offsets becomes almost asymptotically. Again the setup with shift 3 cm seems to be the most stable while still being worse in most offset regimes than more moderate shifts like the optimal shift for both focal lengths.

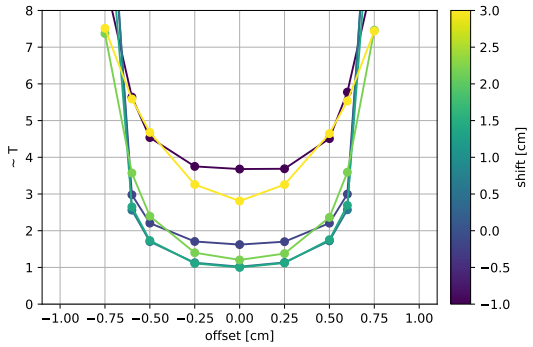

Figure 3.68: Measurement time over offset with a f1 focal length of -6 cm for varying shifts

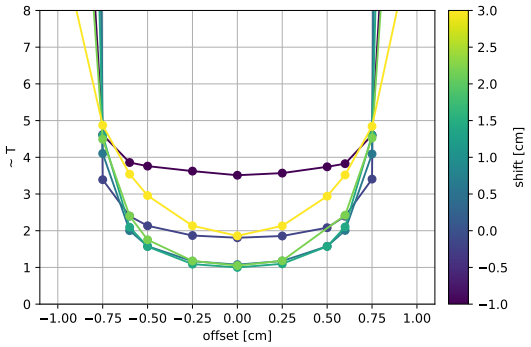

Figure 3.69: Measurement time over offset with a f1 focal length of -7.5 cm for varying shifts

A direct comparison of the measurement times of the optimal setups (see Figure 3.70) reveals that the advantage of the -6 cm focal length lens might possibly neglected by its worse offset performance. Because for offsets bigger than ±0.6 cm the measurement time is greater than for the other lens. This fact becomes more obvious for a larger shift (see Figure 3.71). To assess which lens is preferable a better understanding of the size of the offset is needed.

3.2.5 Focal length converging lens

For further optimization the focal length of the second lens can be changed to adapt for the shift. After re-evaluation of Figures 3.20 and 3.21 room for improvement

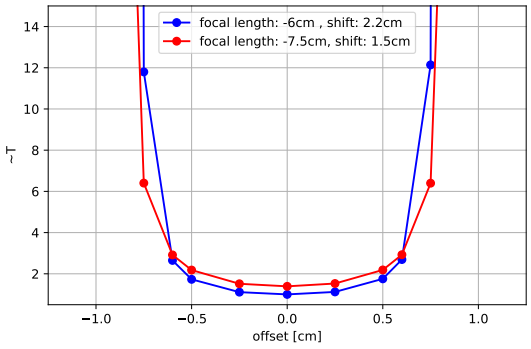

Figure 3.70: Comparison of offset behavior for both lenses with each respective optimal shift

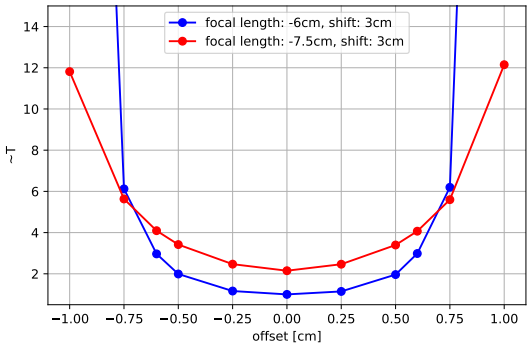

Figure 3.71: Comparison of offset behavior for both lenses with 3 cm shift

becomes apparent. Some rays are focused so strongly that they do not hit the photo detecting area. The reason is that due to the shift most rays have bigger angles to the optical axis and are already somewhat converging. Intuition suggests that a better result can be achieved by implementing a lens with a greater focal distance in such a way that more rays are redirected onto the PMT. The following simulations are all done with a focal length of -7.5 cm of the first lens.
A variety of different converging lenses with different shifts were simulated with a focal length ranging between 5 cm to 40 cm. The ray propagation for 20 cm, 30 cm and 40 cm with a shift of 1.5 cm are shown in Figures 3.72, 3.74 and 3.76. With increasing focal length the waist of the beam gets bigger. But even with just doubling the focal length the overfocusing of rays gets reduced in such a way that the number of rays significantly increases.
If the focal length is increased the size of the ray distribution at the PMT also increases (see Figures 3.73, 3.75 and 3.77).

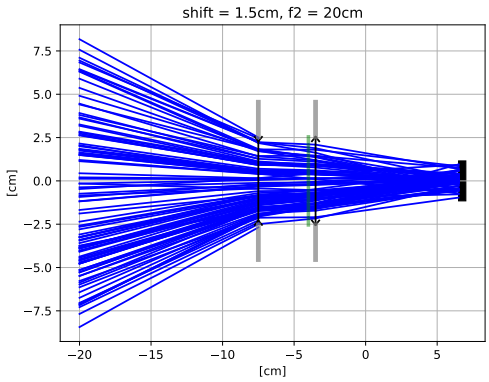

Figure 3.72: Ray trace picture with a shift of 1.5 cm and a f2 focal length of 20 cm

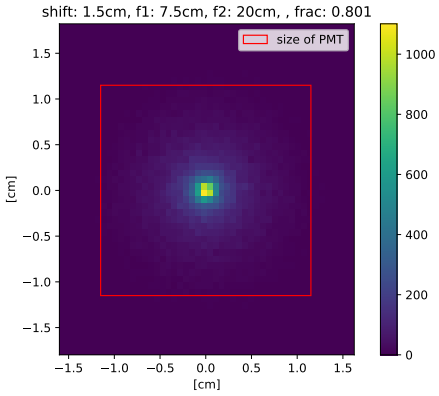

Figure 3.73: Ray distribution at the PMT to the setup with 1.5 cm shift and a f2 focal length of 20 cm

The resulting fractions of surviving rays are shown in Figure 3.78. As expected a smaller focal length does not improve, but worsen the situation. For a focal length of 5 cm the fraction remains below 20% for every shift. An increase in fraction can be seen for focal lengths larger than the initial one of 10 cm.

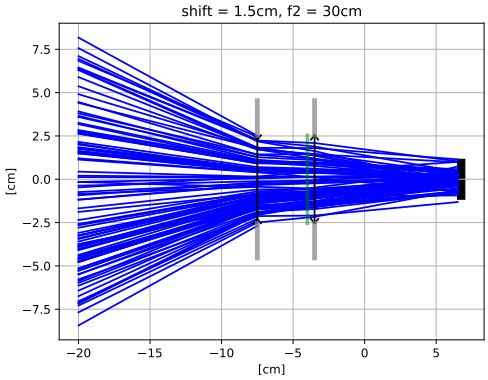

Figure 3.74: Ray trace picture with a shift of 1.5 cm and a f2 focal length of 30 cm

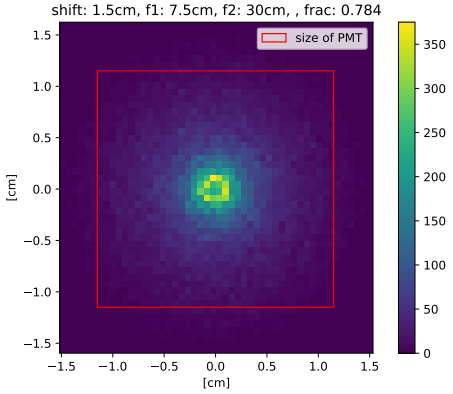

Figure 3.75: Ray distribution at the PMT to the setup with 1.5 cm shift and a f2 focal length of 30 cm

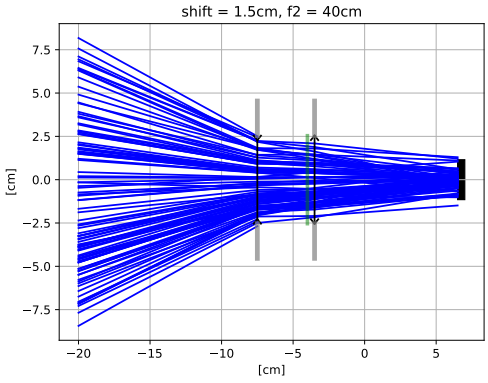

Figure 3.76: Ray trace picture with a shift of 1.5 cm and a f2 focal length of 40 cm

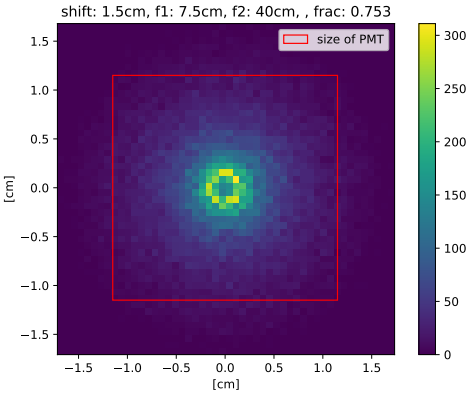

Figure 3.77: Ray distribution at the PMT to the setup with 1.5 cm shift and a f2 focal length of 40 cm

While the maximum for 10 cm focal length occurs as mentioned in the previous section 3.2.2 for a shift of 1.5 cm, the maximum for larger focal lengths occurs for a 2 cm shift. The larger focal length takes effect as expected.

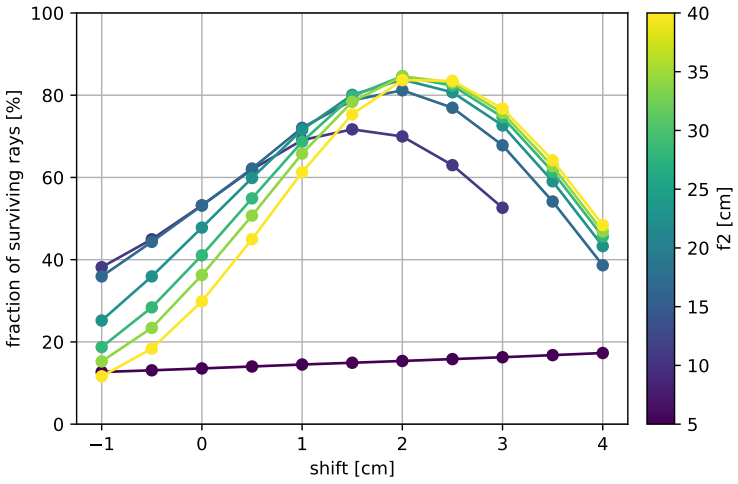

Figure 3.78: Fraction of surviving rays for different shifts and f2 focal length

The choosen focal length of the converging lens has an effect on the distribution of AOIs on the interference filter. Initially this might be surprising because the lens is placed after the interference filter, but the second lens plays an important role in selection of rays which are detected (see Figure 3.78) and therefore subsequently shapes the spectrum by its selective nature. The mean of the distribution for different focal lengths and shifts is shown in Figure 3.79. The 10 cm focal length curve is identical to Figure 3.29. The larger focal length has got a smaller mean for negative and zero shift. This changes starting at 0.5 cm shift until the mean is about 1° greater at 3 cm shift.
The standard deviation of the angular distribution seen in Figure 3.80 has the shape as mentioned before, but for larger focal length the maximum is about 0.5° bigger.
Both increases are explained by the fact that the rays that hit the detector due to the larger focal length are the rays with more extreme AOIs.
The measurement time as factor of the quality of the system is shown in Figure 3.81. For small -1 cm shift only the setup with 10 cm shows a reasonable measurement time which is still over a factor 4 larger than the minimum. The minimum for the 10 cm curve is as the plot of the fraction (see Figure 3.78) indicates at 1.5 cm shift. The other setups have their minimum at a shift of 2 cm.
That suggests that a setup with a bigger focal length of the converging lens might be more sufficient than the used 10cm lens. But as previous discussed in Section 3.2.4 a setup also has to be stable against a possible offset. That is why the setups are investigated for their stability.
For this only the optimal shifts are taken into account and exposed to increasingly big offsets. The optimal shift is 1.5cm for the 10 cm lens and 2 cm for the other lenses. The fraction of surviving rays (see Figure 3.82) shows that the 10 cm lens while producing a smaller percentage is more stable to offset. For offsets starting

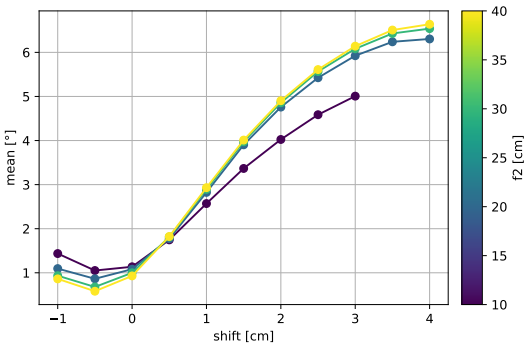

Figure 3.79: Influence of the f2 focal length on the mean of the angular distribution

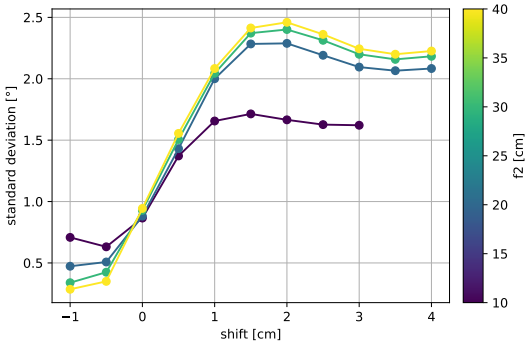

Figure 3.80: Influence of the f2 focal length on the standard deviation of the angular distribution

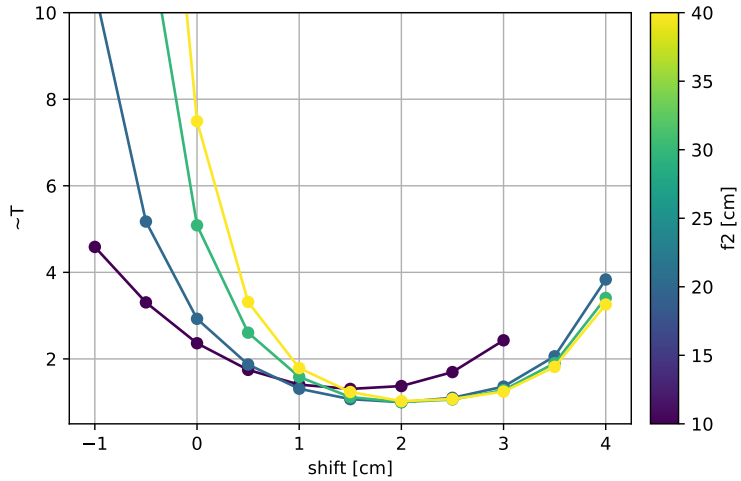

Figure 3.81: Search for optimal f2 focal length and shift

by ±0.5 cm it shows a larger fraction than the other lenses which show a drastic decline for shifts larger than ±0.25 cm. The setups with 30 cm and 40 cm have very similar outlines while the setup with 20 cm lies in between 10 cm and the other lenses. Again all setups are symmetrical to the sign of the offset.

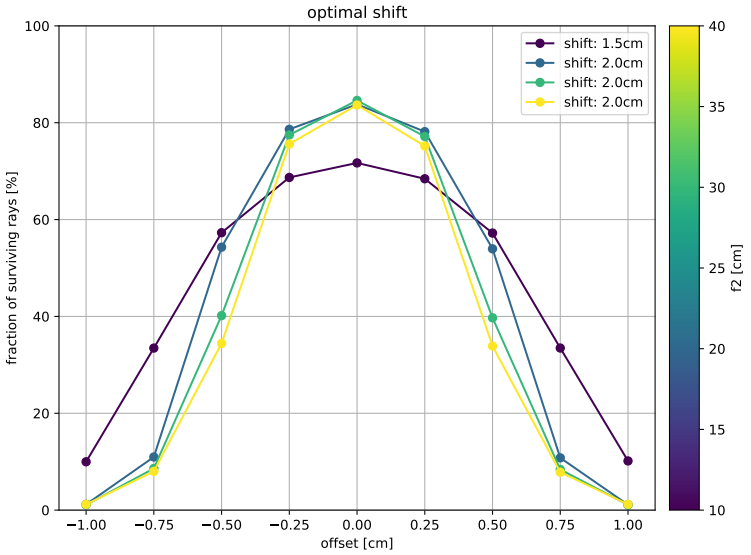

Figure 3.82: Test of stability in respect to the fraction of surviving rays of the setups with different f2 focal length

Again the deciding factor in the measurement time is the fraction of surviving rays (see Figure 3.83). T is smallest for the setups with 30 cm and 40 cm for small offsets, but is similar to the fraction overtaken by the 10 cm setup for offsets bigger than ±0.25 cm.

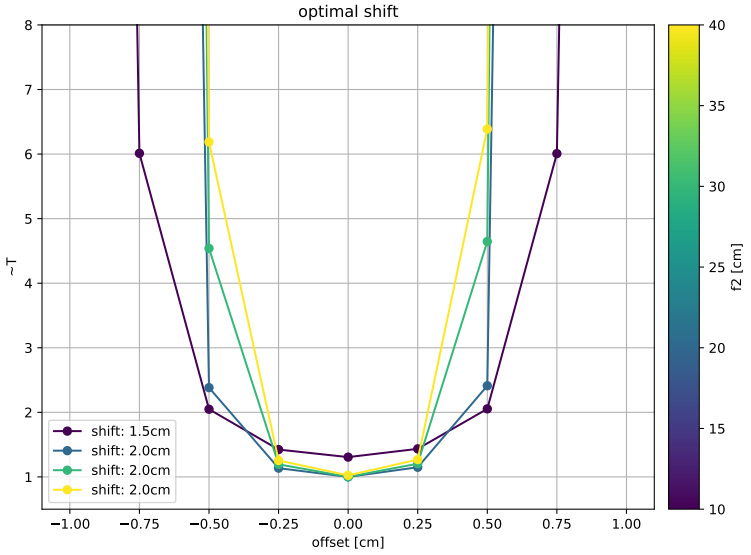

Figure 3.83: Test of stability in respect to the measurement time of the setups with different f2 focal length

3.3 Summary H.E.S.S. simulation

The interferometry setup for the 12 m H.E.S.S. telescope consists out of multiple components which have an influence on how the rays are propagated through the system. The differences in these setups affect the produced spectra and therefore also the properties of the measurement, the measurement time to get a signal with a certain significance. A simulation of the path the light bunch, provided by the H.E.S.S. telescope, takes allows to test out a variety of different components with different properties and also changes the distance ratio to each other. The simulation used a form of tracing rays by which each ray interacts with the objects it encounters on its light path: sequential ray tracing. A special interest was taken into the AOIs of the rays on the interference filter in the middle of the setup because those influence the spectrum that is measured.
Because a simulation is used, different setups with different components and spacing can be tried out and optimized. Since every component and value influences each other mutually a multidimensional optimization was needed.
The first property that was investigated is the shift of the entire interferometry system to the focal point of H.E.S.S. in Section 3.2.2. The result was that a shift of 1.5 cm is optimal for all three filters that were used (see Figures 3.33, 3.35 and 3.36). In comparison of the interference filter in measurement time and coherence time it turned out that the Alluxa filter with 2 nm width and a central wavelength of 465 nm is the best for the setup and improves the measurement time by a factor of at least 1.15 (see Figure 3.38) and the coherence time by a factor of roughly 5 compared to the other filters (see Figure 3.39). This confirms that the coherence time is inverse proportional to the bandwidth.
The shift result leads to the realization that a smaller focal length of the diverging lens at the begin of the setup might be helpful. Therefore an examination of the effect the changed focal length of -6 cm takes on the system was conducted in Section 3.2.3. The setup was tested for changing shifts and the results were compared to the previous results with a focal length of -7.5 cm (see Figure 3.50). The optimal shift for the changed focal length proved to be 2.2 cm. With the different focal length the best value for the measurement time could indeed be improved by a factor of 1.39.
For a final conclusion whether this lens is actually superior to the other the behavior of the system under an offset that might emerge because of inaccurate pointing of the telescope was investigated in Section 3.2.4. It became obvious that an offset has a massive effect on the measured data. For big offsets the measurement time almost diverged and was multiple factors larger than the best value with no offset (see Figures 3.68 and 3.69). It also became clear that depending on the size of the offset a setup with 3 cm shift might be beneficial. In the direct comparison the setup with 7.5 cm focal length seems to be more stable for offsets larger than $\pm$0.6cm (see Figures 3.70 and 3.71).
It became apparent that some rays miss the PMT at the end of the setup, because they are focused to much. Different larger focal length for the converging lens were tested out in Section 3.2.5. The enlarged focal length indeed proved to be beneficial to the fraction of surviving rays (see Figure 3.78) as well as for the measurement time (see Figure 3.81) where the minimum shifted to 2 cm shift and

a focal length of 20 cm (focal lengths 30 cm and 40 cm are only marginally worse) and a value that was 1.37 times smaller than for the initial focal length of 10 cm. As before the effect of offset to the system was tested (see Figure 3.83). The offset has a strong influence on the measurement time especially for longer focal length. The 10 cm lens proves to be most stable starting with a offset of ± 0.5 cm.
To make the best decision which setup to use a thorough investigation on how precise the H.E.S.S. pointing is and how often and how big offsets occur, is needed.

4 Intensity interferometry with IceAct

4.1 Optics used in IceAct

The Ice Imaging Air Cherenkov Telescope (IceAct) are small-sized Imaging Air Cherenkov Telescopes which are planned to be located above the IceCube detector in Antarctica. Their main goal is to function as a muon veto for the IceCube neutrino detector. One telescope (see Figure 4.1) has a diameter of 55 cm and a length of 1 m including the data aquisition (DAQ)[23]. Unlike the H.E.S.S. telescope IceAct telescopes are rather small and inexpensive. The system planned for the interferometry setup consists of its Fresnel lens, a tube, an interference filter and a photo detector. The setup uses an interference filter with 22 mm clear aperture and 36 nm bandwidth spectrum at 432.1 nm central wavelength [24]. This broad filter is used because of the small size of the telescope parallelization can not be achieved with reasonable effort. The wider filter spectrum produces a similar signal to noise ratio as a narrower filter.

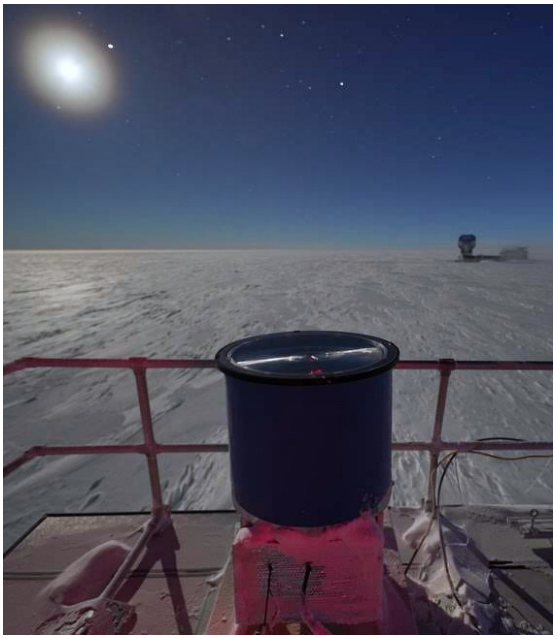

Figure 4.1: Picture of a IceAct prototype telescope in operation[23]

4.1.1 Fresnel lens

A Fresnel lens is a concept of a lens that allows refraction of light within a more compact form. This can be accomplished by cutting out major parts of a spherical lens and stacking together the remaining approximated linear segments of the lens in grooves (see Figure 4.2).
These grooves contain an active and an inactive face (see Figure 4.4). The active face is characterized by the slope angle δ which is determined by the linear

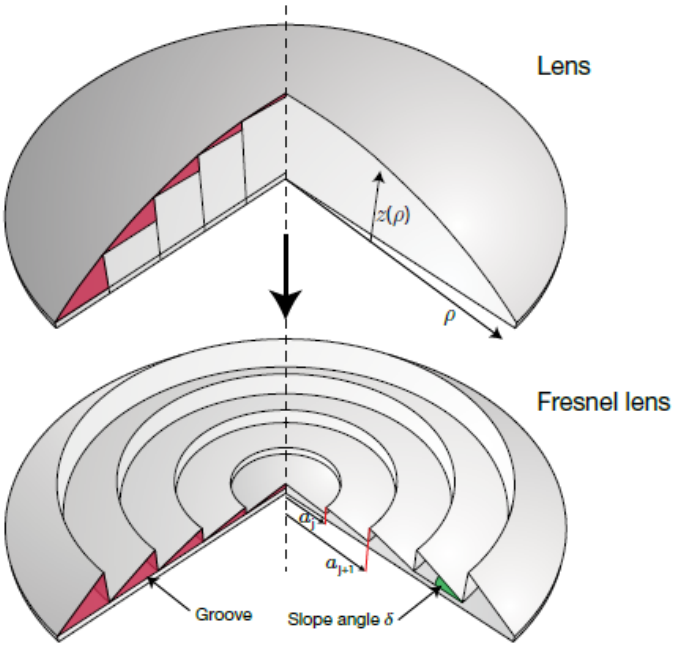

Figure 4.2: Illustration of how a Fresnel lens can be constructed out of a spherical lens with equal focal distance [25]

approximation of the sagitta function of the spherical lens:

$$z(\rho) = \frac{c \cdot \rho^2}{1 + \sqrt{1 - (k+1) \cdot c^2 \rho^2}} + \sum_{i=1}^{O} A_{2i} \rho^{2i} [26] \tag{4.1}$$

Equation 4.1 calculates the thickness of a thick lens depending on $c = \frac{1}{R}$ with R the radius of curvature, the distance to the center of lens and k the conic constant. The sum in the second part of the equation gives the opportunity for aspheric surfaces with $A_i \neq 0$.
The radius of curvature for a given lens can be calculated via Equation 4.2. It is assumed that the optical transition is from air to lens material and back.

$$\frac{1}{f} = (n-1) \left[\frac{1}{R_1} - \frac{1}{R_2} + \frac{(n-1)d}{nR_1R_2} \right] [4, \text{ p. } 261] \tag{4.2}$$

For a plano-convex lens the radius of curvature of the backside R_2 goes to infinity which further simplifies the equation:

$$\frac{1}{f} \overset{R_2 \to \infty}{=} (n-1) \left[\frac{1}{R_1} \right] \Rightarrow R_1 = (n-1) \cdot f \tag{4.3}$$

with f the focal length of the lens and n the refractive index of the lens material. The conic constant k in Equation 4.1 gives an impression of the profile of the lens. Different variants of the conic constant can be seen in 4.3

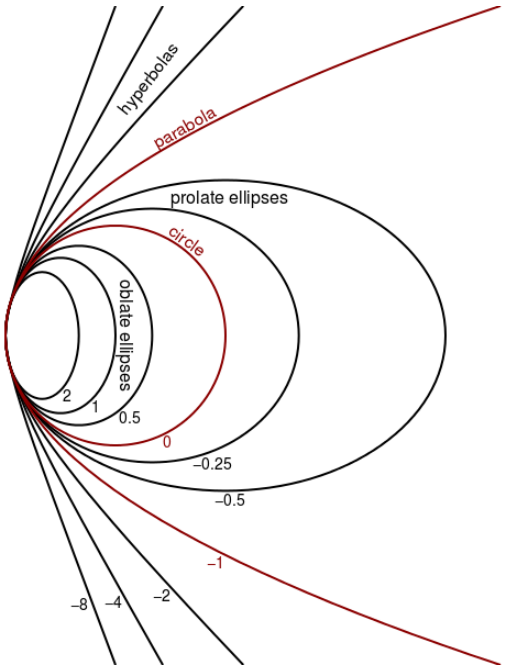

Figure 4.3: Illustration of various conic constants[27]

The characterization of the inactive face is given by the draft angle ψ.

$$\psi(\rho) = 3° + 0.0473° \,\mathrm{mm}^{-1}\rho[28] \tag{4.4}$$

There is a transition phase between the active and inactive phase of the lens where the ideal theoretical peak is rounded.
The Fresnel lens used in IceAct is the positive Fresnel lens SC943 from Orafol [29]. It is made out of polymethylmethacrylate (PMMA), has a focal length of 502.1 mm for $\lambda = (546 \pm 27)$ nm and a groove distance of 0.1 mm with a clear aperture of 549.7 mm and a thickness of 2.5 cm.
Not all rays that hit a lens will get refracted in the intended way. Some will hit the draft face and are refracted outwards and some will hit the lens at an angle that is greater or equal to the critical angle of total internal reflection given by:

$$\frac{n_2}{n_1} \overset{\text{with } n_1 > n_2}{=} \sin\alpha_c[4,\ \text{p. } 226] \tag{4.5}$$

with n_1 and n_2 the refractive indices of the two layers (air and lens material) and α_c the critical angle. This means if the slope of a lens is greater than α_c the incoming rays are no longer refracted and transmitted, but reflected.

4.2 Ray tracing simulation of IceAct

The sequential ray tracing simulation for IceAct was done in Python. At the beginning 3,807,420 rays were created equally and randomly distributed up to a radius which is equal to half the clear aperture of the Fresnel lens (see Figure 4.5). Radii which are larger than this were not taken into account, since only light rays parallel to optical axis were used, so any rays with a bigger radius would not

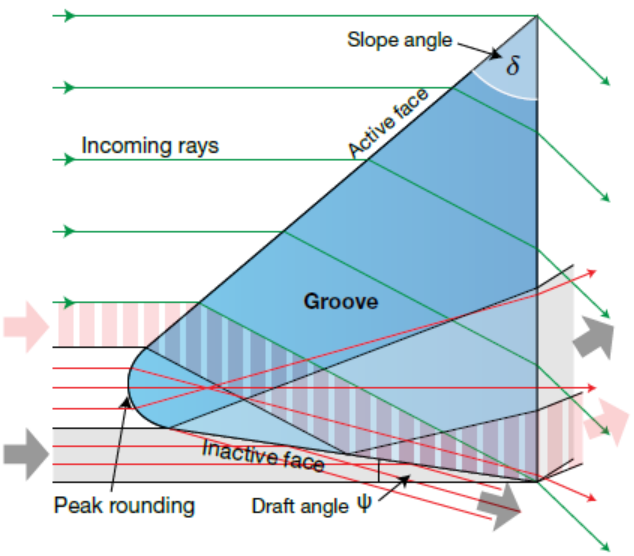

Figure 4.4: Illustration of the groove profile of a Fresnel lens[25]

end up in the IceAct telescope. The consideration of only parallel incoming light is approximately true, since the mounts and audio guiding software used, works sufficiently well. Therefore effects for non parallel light do not need to be taken into account.

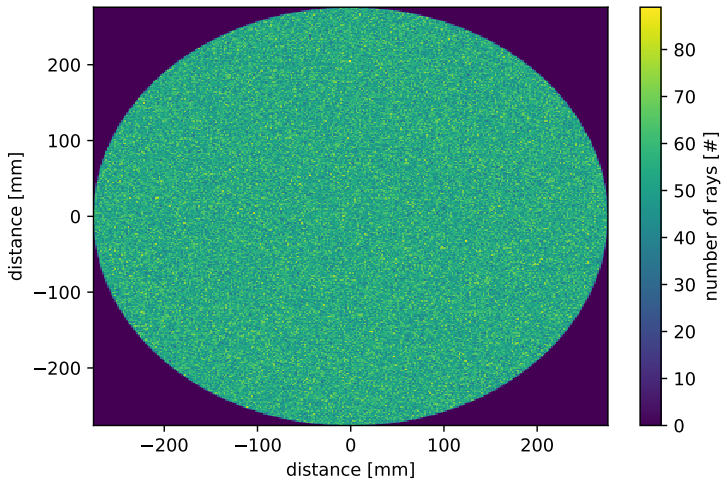

Figure 4.5: Depiction of initial light distribution

The data of one ray consist of the distance to the optical axis ρ, its angle around the optical axis ϕ, its elevation above the lens z and its angle to the optical axis α. All the incoming light also gets appointed a wavelength. This is done because the refraction index is wavelength dependent $n = n(\lambda)$.

4.2.1 Ray tracing through Fresnel lens

Before the properties of the Fresnel lens could be calculated some other variables need to be determined. The radius of curvature was calculated using Equation

4.2 while using the Sellmeier equation 4.6 to determine the wavelength dependent refractive index $n(\lambda)$.

$$n^2(\lambda) = 1 + \frac{B_1\lambda^2}{\lambda^2 - C_1} + \frac{B_2\lambda^2}{\lambda^2 - C_2} + \frac{B_3\lambda^2}{\lambda^2 - C_3} [30]$$
$$\Rightarrow n(\lambda) = \sqrt{1 + \frac{B_1\lambda^2}{\lambda^2 - C_1} + \frac{B_2\lambda^2}{\lambda^2 - C_2} + \frac{B_3\lambda^2}{\lambda^2 - C_3}} \tag{4.6}$$

Before that can be done the Sellmeier coefficients B_i and C_i have to be determined. For that the data from [31] were fitted with Equation 4.6.

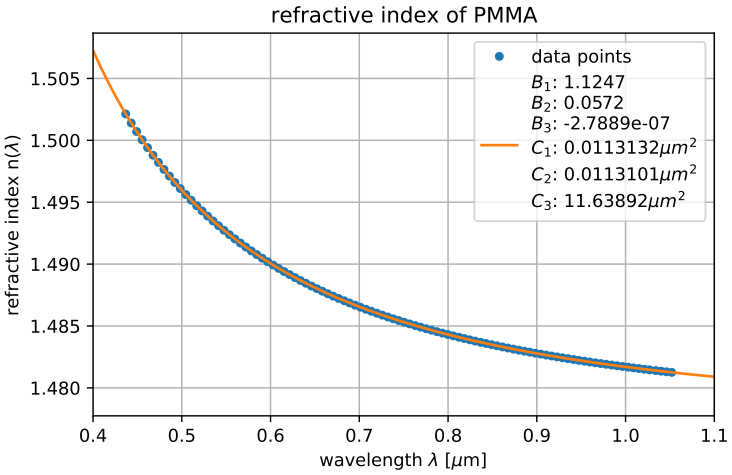

Figure 4.6: Fit of refractive index data to get Sellmeier coefficients of PMMA [31]

The results of that fit are displayed in Table 4.1.

B_1	1.12469967
B_2	0.0572003025
B_3	$-2.78891343 \cdot 10^{-07}$
C_1	0.0113131540 μm^2
C_2	0.0113100621 μm^2
C_3	11.6389208 μm^2

Table 4.1: Sellmeier coefficients for PMMA calculated by fitting the data

The refractive index for the lens is determined for a wavelength of 546 nm because that is the area in which the focal length is set [29]. This gives the refractive index for PMMA:

$$n_{\text{PMMA}}(546\,\text{nm}) \approx 1.493. \tag{4.7}$$

For creating the lens data of the Fresnel lens the thickness of a spherical lens with the same focal length 502.1 mm and clear aperture 549.7 mm was calculated using Equation 4.1. This was done for different conic constants (see Figure 4.7).

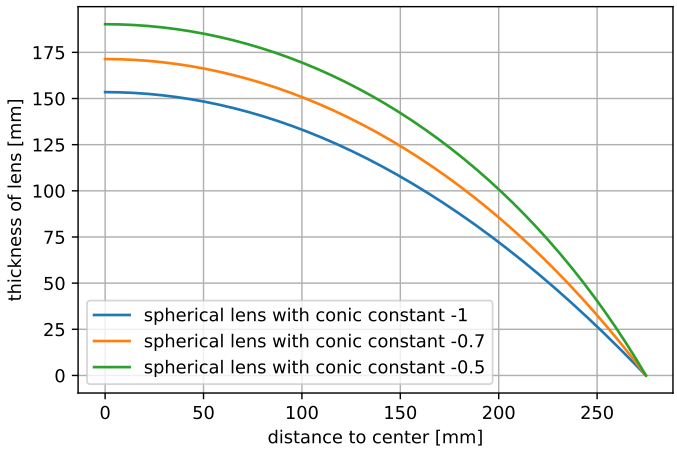

Figure 4.7: Profile of spherical lenses with different conic constants

The lens gets flatter at the top close to the middle of the lens if it has a larger conic constant. After the thickness is known in dependency of the distance to the lens center, the slope between points of the surface can be calculated with a spacing of 0.1 mm. This slope represents the linear approximation of the actual slope between these points. The slope angle in dependency of the distance to the center can now be used to characterize the Fresnel lens. The thickest point of a groove is 2.5 mm thick. Combined with the known distance between two grooves of 0.1 mm the thickness and slope of the Fresnel lens can be determined for the entire lens because each groove can be viewed as a right triangle.
In reality this is an idealized representation of the groove. Because of constraints in the manufacturing process there is peak rounding as well as an inactive draft face characterized by Equation 4.4. The used simulation does not incorporate peak rounding. However the draft face as a complement of the active slope face is implemented. The profile is characterized by the slope angle on the one side and by the draft angle on the other side (see Figure 4.8).
The groove distance d is equal to the width of a single groove. It can be splitted into the width of the slope face b and the width of the draft face a. Their values can be calculated by:

$$b = \frac{d}{1 + \tan\delta \tan\psi}$$
$$a = \frac{d}{1 + \frac{1}{\tan\delta \tan\psi}} \text{[25]} \tag{4.8}$$

For the lens profile a and b are determined for each groove depending on slope angle δ and draft angle ψ. The middle point in between a and b is calculated and its width is set to 2.5 mm. If this is done the profile is calculated towards the edges using δ and ψ. This leads to the thickness profile of the Fresnel lens with an inactive face. The thickness profile of an ideal Fresnel lens as well as a Fresnel lens with draft face is depicted in (see Figure 4.9) for conic constant of -1.

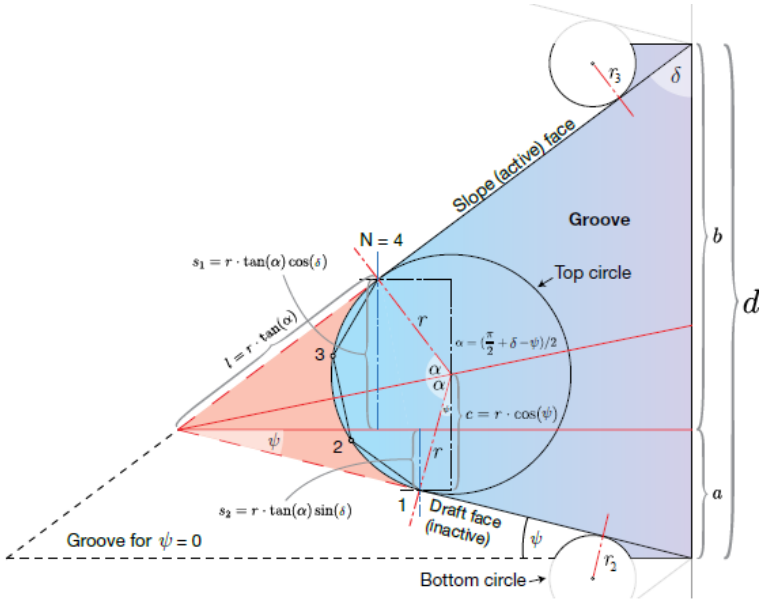

Figure 4.8: Representation of a realistic groove profile with groove distance d = 0.1 mm[25]

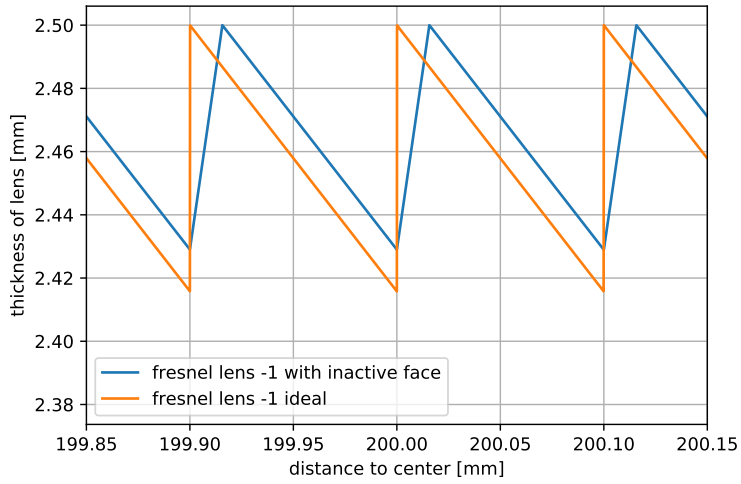

Figure 4.9: Part of thickness cross section of an ideal Fresnel lens (orange) and a Fresnel lens with inactive draft face (blue). Both calculated with a conic constant of -1.

Because the non ideal lens has two sides, it is thicker at the thinnest point compared to the ideal lens.

After the lens' profile data are calculated they are put into the ray tracing simulation. The light data (see Section 4.2) are placed at a starting point in front of the telescope and then gets propagated in direction of the lens. For that the z value of each ray gets set to the next component of the telescope while simultaneously calculating the new distance to the optical axis ρ using its angle to the optical axis.
If the light encounters the lens all rays are still parallel to each other as well as to the optical axis. Each ray encounters the lens at a different value of z according to the rays distance to the optical axis and the fitting lens profile thickness for the same distance. Then the simulation checks whether the ray hits a draft face or if it hits the slope face. In either way the ray gets appointed the angle of the slope or draft angle it hits on the lens. The simulation takes the angle between the optical axis and the slope or draft angle. The draft angle is interpreted as a negative angle so that rays get refracted outwards. For slope angles greater than the critical angle for total reflection α_c the rays are reflected and dismissed in the next steps. The monotonous increasing slope allows to determine a critical distance to the center of the lens at which every ray is reflected and not transmitted. For all the other rays the wavelength dependent refractive index $n(\lambda)$ is calculated.
The refraction process is simulated by using Snell's law in following equation:

$$\alpha_{\text{out}} = \arcsin\left(\frac{n_{\text{in}}}{n_{\text{out}}} \sin \alpha_{\text{in}}\right). \tag{4.9}$$

The angle α_{out} is assigned as the rays' new angle to the optical axis. If this is done the rays gets propagated according to their angles α to the other side of the lens, where they are once again get refracted by the transition from PMMA to air. Once again their angle to the optical axis changes and they are propagated further to a variable chosen distance to form a focal spot. The whole process of the ray tracing is depicted in Figure 4.10 in a 3D view and in Figure 4.11 in a 2D view.
The simulation of the lens produces an expected behavior: Most of the rays get focused inside a relative small area, the focal spot, some rays get refracted outwards because they hit the draft face and there is an area where no rays are refracted because they get totally reflected.
The focal spot and especially its size is characterized by its spread and the distance to the center. Therefore, the value of the aberration radius R90 is introduced. R90 describes the 90%-quantile of the rays, hence the radius inside which 90% of rays reside.

4.2.2 Conic constant of lens

As previously mentioned the Fresnel lens is characterized by a spherical lens using Equation 4.1. All variables of the relation are given or can be calculated, except the conic constant.

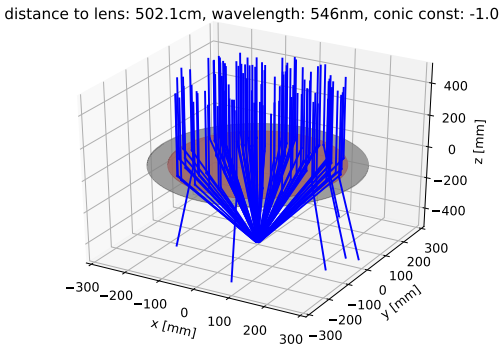

Figure 4.10: 3 dimensional ray trace picture with a wavelength of 546nm and a conic constant of -1 propagated to a distance of 502.1mm. The grey area is the size of the lens while the red area is the maximal radius where no total internal reflection appears, hence the part of lens where rays are refracted and not totally reflected.

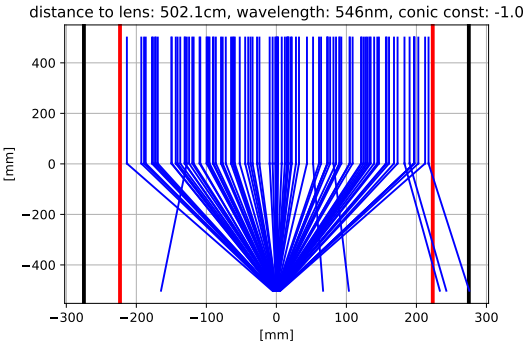

Figure 4.11: 2 dimensional ray trace picture with a wavelength of 546nm and a conic constant of -1 propagated to a distance of 502.1mm. The red lines show the maximal radius to the center of the lens where rays are still refracted. The black lines show the actual clear aperture of the lens.

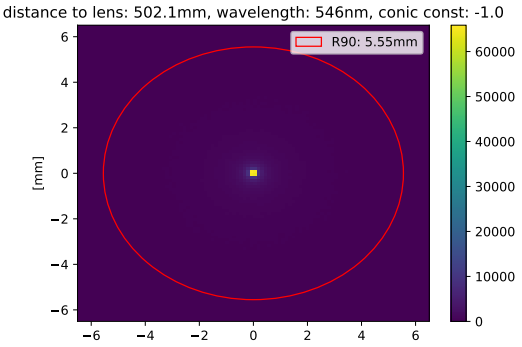

Figure 4.12: View of the focal spot with 502.1 mm distance to the lens and conic constant of -1 using light with wavelength 546 nm.The red circle shows the aberration radius R90

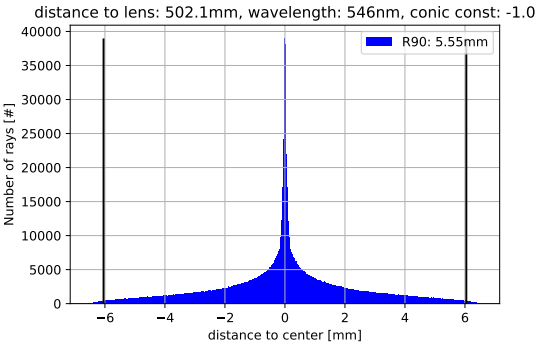

Figure 4.13: Distribution of the focal spot in one dimension with 502.1mm distance to the lens a conic constant of -1 and the wavelength 546 nm. The black lines represent R90

The conic constant has a clear influence on the behavior of the lens. For once the slope angle differs especially for increasing diameter (see Figure 4.14). For -1 the slope angle increases almost linear apart from a slight flattening for high diameters, while for -0.189 this is just true for smaller diameters and for larger ones it increases clearly until it reaches the maximum at 90°.

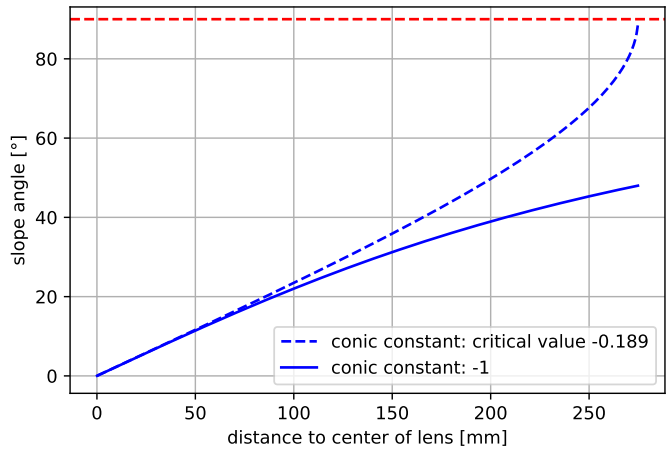

Figure 4.14: Comparison of the slope of Fresnel lenses with conic constants -1 (blue line) and -0.189 (dashed blue line). The maximal possible slope angle of 90° is depicted by the red dashed line.

The different slopes not only change how rays with large distance to the center are refracted, but also change at which diameter total internal reflection starts (see Figure 4.15). For increasing conic constant the minimal diameter for total reflection decreases because the slope is larger for theses lenses.

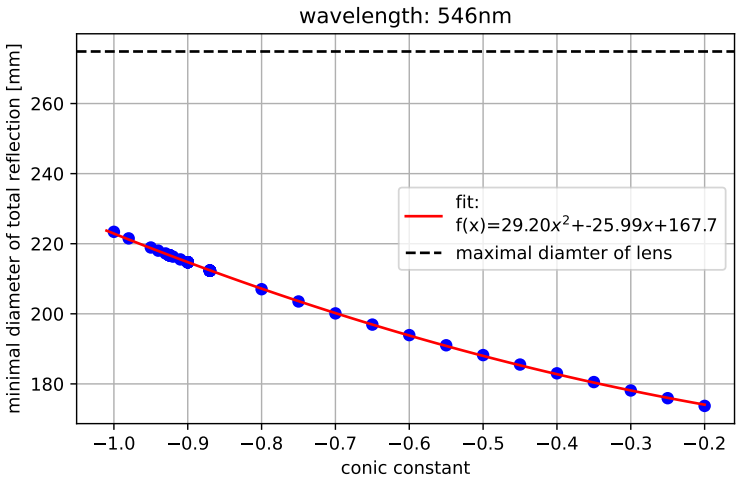

Figure 4.15: Relation between conic constant and fraction of surviving rays

Another aspect that is influenced by the conic constant and is related to the slope angle is the overall ratio between the active and inactive face of the lens. A

theoretical comparison between both faces for different conic constants is shown in Figure 4.16. Close to the center of the lens there is almost only an active face for -1 as for -0.189. For larger diameters this changes. With the conic constant there is just a small decrease in active face while for -0.189 the ratio flips.

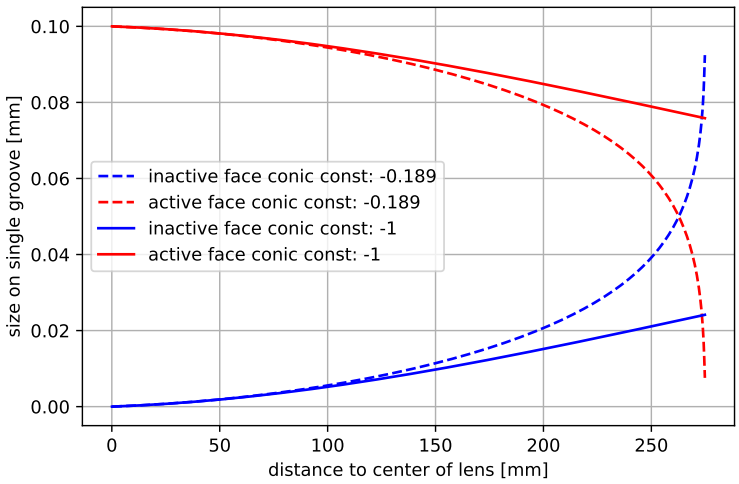

Figure 4.16: Difference in size of active b and inactive face a (see Figure 4.8 and Equation 4.8)

The ratio b/a together with the slope and therefore the minimal radius for total reflection are both affected by the conic constant. This leads to the conclusion that the fraction of surviving rays depends on the conic constant (see Figure 4.17).

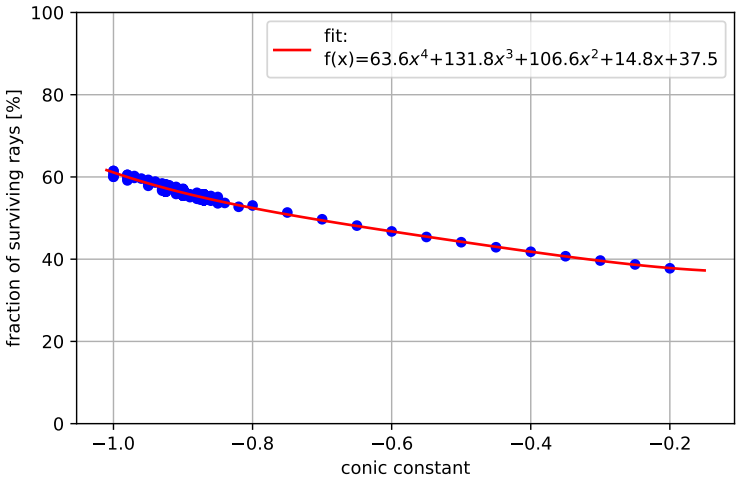

Figure 4.17: Relation between conic constant and fraction of surviving rays

The relation between fraction and conic constant can be described well by a polynomical function of 4-th order. Because the constant is unknown a reasonable value has to be found.
Assuming the Fresnel lens is based on a spherical lens with no aspherical parts Equation 4.1 becomes:

$$z(\rho) = \frac{c \cdot \rho^2}{1 + \sqrt{1 - (k+1) \cdot c^2 \rho^2}}. \tag{4.10}$$

Because the clear aperture of the lens is given with 549.7 mm a conic constant of zero is not realistic, because then the radius of curvature is smaller than half of the clear aperture. The maximal conic constant for a given radius of curvature can be calculated by deriving Equation 4.10. This leads to:

$$\frac{d}{d\rho} \frac{c \cdot \rho^2}{1 + \sqrt{1 - (k+1) \cdot c^2 \rho^2}} = \frac{c\rho}{\sqrt{1 - (k+1) \cdot c^2 \rho^2}} \tag{4.11}$$

The critical point is given by the critical point of that equation:

$$\begin{aligned} 1 - (k+1) \cdot c^2 \rho^2 &\stackrel{!}{=} 0 \\ \Rightarrow k_{\text{crit}} &= \frac{R^2}{\rho^2} - 1 \end{aligned} \tag{4.12}$$

The maximal conic constant k_{crit} of the used Fresnel lens has got a value of $k_{\text{crit}} \approx -0.189$. So there is an upper constraint for conic constant, but there is no intrinsic lower bound.
To determine the actual constant, three known values were taken:

origin	wavelength [nm]	distance to lens [mm]	best conic constant
measurement with own lens	432	488	-0.87
measurement with own lens	465	494	-0.9
statement of manufacturer	546	502.1	-0.925

Table 4.2: Known properties of the lens used to find conic constant

The measurements of these values were conducted by Andreas Zmija, Adrian Zink and Jigar Bhanderi at Erlangen Centre for Astroparticle Physics (ECAP) with the IceAct telescope pointing at Sirius. For the measurement of the lens an interference filter of 432 nm and 465 nm was placed in the light path as well as a pinhole with 5 mm diameter right in front of the PMT . The pinhole with the PMT was then moved to different distances to the lens and the signal would measure a maximal photo current if the PMT was in the focal point.
This information was used and the simulation was started with the set wavelength. The focal point was then taken at the respective distance and for that the aberration radius was calculated. This was done with a variation of conic constants (see Figure 4.18).
The position of the minimum of each curve is the conic constant that matches the observation best (see Table 4.2). The three different values for $k = -0.925, -0.9, -0.87$ seem to be in disagreement, but there are uncertainties on each value. For the value derived from the manufacturer's statement there is a $\pm 5\,\%$ margin of error on the used wavelength. For the own measurement the filters are not strictly monochromatic especially if the shift of the filter function due to AOIs $\neq 0°$ is

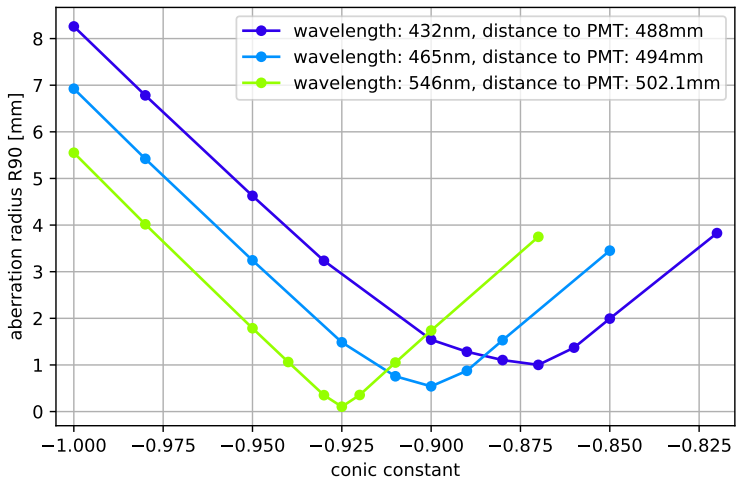

Figure 4.18: Aberration radius at set distance and wavelength for varying conic constants

considered. Another issue is that the pinhole had a diameter of 5 mm which is not sufficient in distinguishing in focal points smaller than that.
A measurement of the lens' R90 with a wavelength of 550 nm at a distance of 513 mm was done in [28].
The measured value was R90 = $(3.24 \pm 0.03(\text{stat})^{+0.65}_{-0.43}(\text{sys}))$ mm. The comparison of the values simulated with different conic constant (see Figure 4.19) shows that the simulation values for former derived conic constants are of the same magnitude, but not in the error range. The additional values are produced by possible deviations of the wavelength. This means (546±27) nm for the statement of the manufacturer and (432±18) nm for the interference filter measurement. The value that comes closest is the one with a conic constant of -0.94 which produces R90 = 3.31 mm.

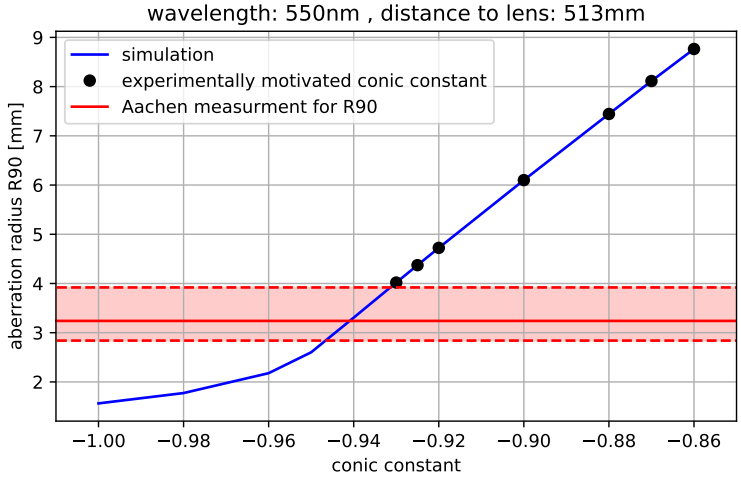

Figure 4.19: Comparison of the simulation results to the measured result of the Fresnel lens for light with 550 nm wavelength and a distance of 513 mm

Because a clear decision on which conic constant should be used can not be made, the behavior of the lens for each is investigated. Figures 4.20, 4.21 and 4.22 show the chromatic aberration of the lens for different conic constants. As for a classical lens shorter wavelength have a shorter focal length than light with longer wavelength. This means that there is not one focal spot, but a different one for each wavelength of the spectrum at increasing distances.

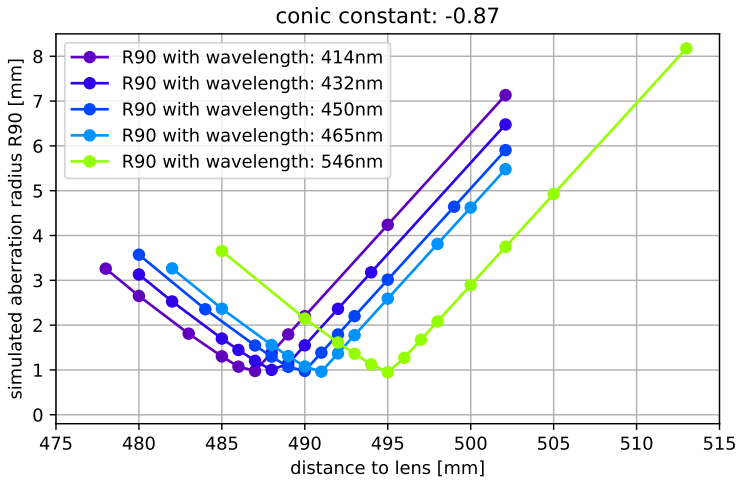

Figure 4.20: Size of R90 for varying wavelength and distances with a conic constant of -0.87

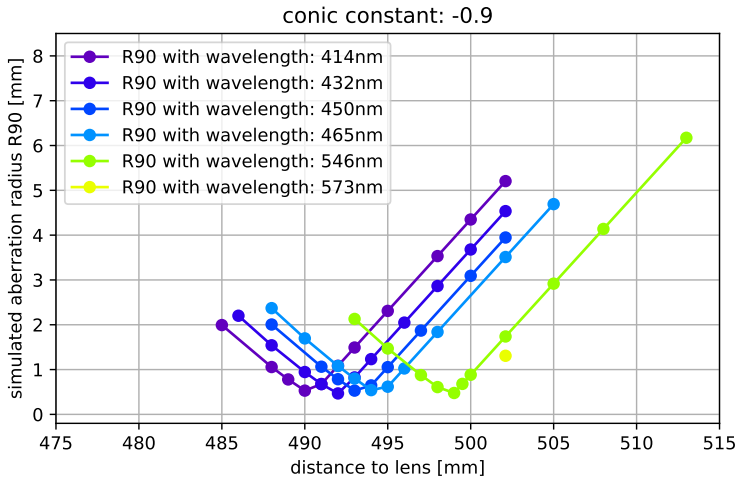

Figure 4.21: Size of R90 for varying wavelength and distances with a conic constant of -0.9

The distance of the smallest R90 increases with wavelength (see Figure 4.23) because of the decreasing refractive index (see Equation 4.6).
The conic constant leads to an offset to larger distances for smaller constants. The shape and distances between the different wavelengths do not change significantly.

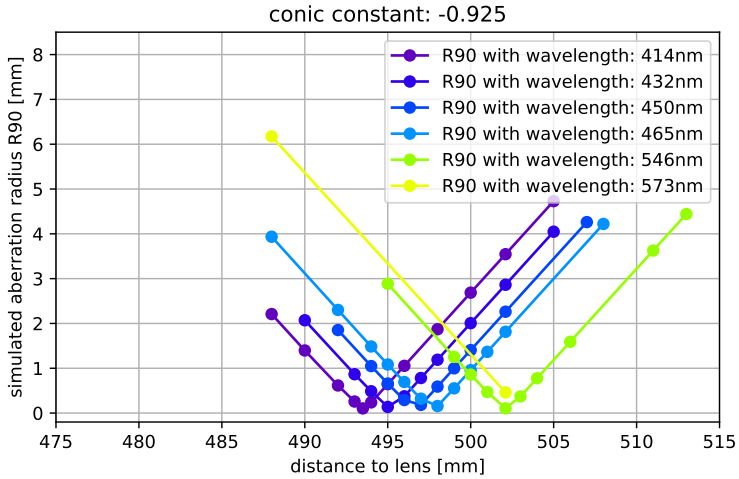

Figure 4.22: Size of R90 for varying wavelength and distances with a conic constant of -0.925

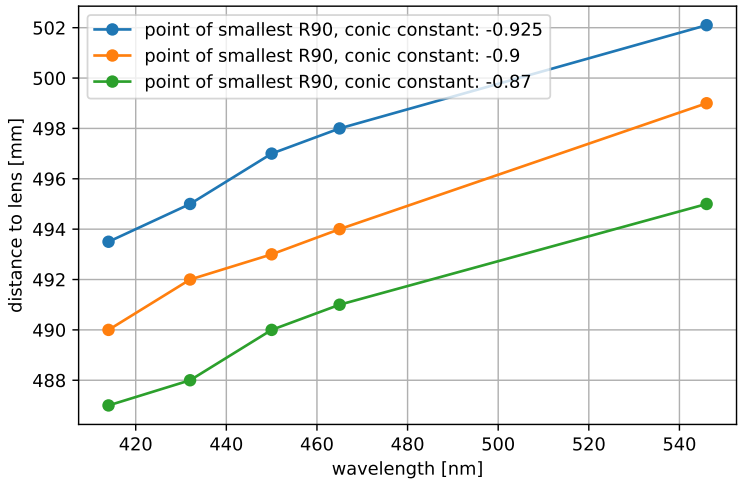

Figure 4.23: Distance of the focal points for different wavlengths and conic constants

4.2.3 Spectrum produced in IceAct

For the IceAct stellar intensity interferometry measurements there are no additional lenses after the Fresnel lens. The rays, after they are focused go directly to the interference filter and the PMT. The light encounters the interference filter in a wide variety of AOIs (see Figure 4.24). The mean of the distribution with conic constant -0.87 is 15.57°.

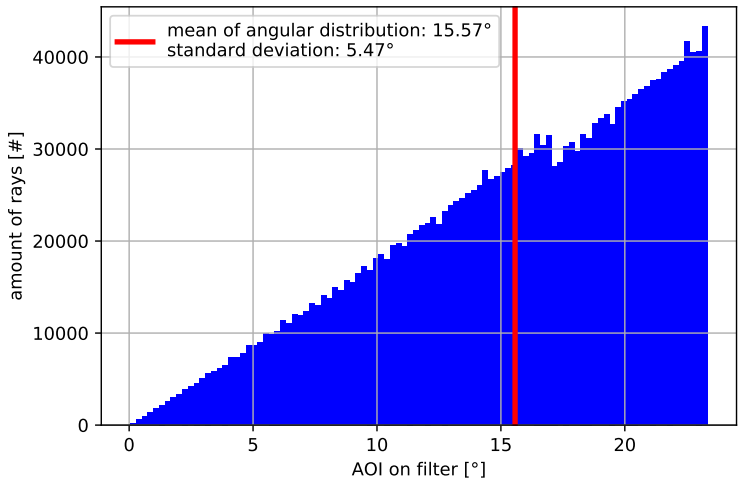

Figure 4.24: Angular distribution of rays at the interference filter for the IceAct telescope simulated with a Fresnel lens with conic constant -0.87 and light with a wavelength of 432 nm at a distance of 488 mm

To counter the differences in AOI a band pass filter with a width of 36 nm and central wavelength of 432 nm is used [32]. Compared to the H.E.S.S. setup this filter is clearly wider (compare Figures 3.30 and 4.25). As before for the H.E.S.S.

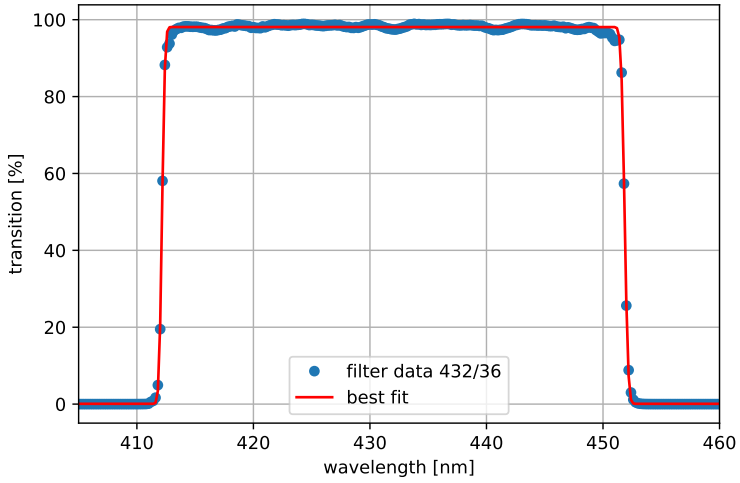

Figure 4.25: Transmission function of a Semrock bandpass filter with 36 nm and a central waelength of 432 nm [32] approximated by a rectangular function

setup a combined spectrum is produced by adding up the single spectrum of each

ray in the light bunch and normalizing the resulting spectrum by division of the number of rays.
This is done for three different conic constants at a wavelength of 432nm (see Figure 4.26).

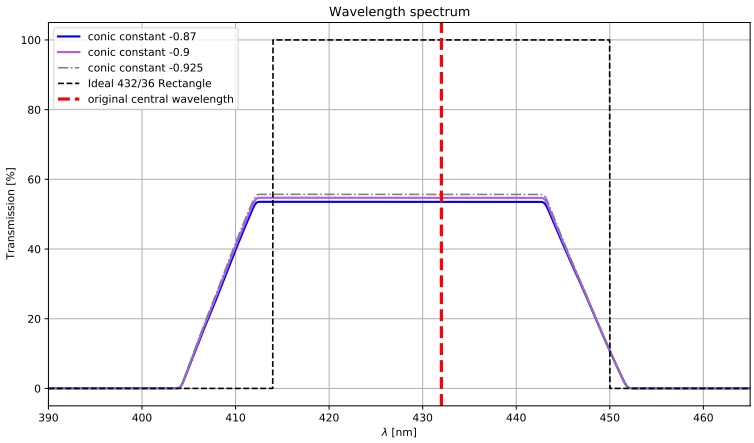

Figure 4.26: Spectra of rays produced with different Fresnel lenses with different conic constants and an ideal rectanlge for comparison

The resulting spectra do not differ much. The edge is marginally steeper for smaller conic constants and the transition percentage is also slightly higher for these constants. Both effects can be explained by the early onset of total reflection for the Fresnel lens with a bigger conic constant and therefore larger slope (see Figure 4.14). The combined spectra are shaped like a trapezoid. The originally steep edges of the rectangular filter function have clear visible slope. The central wavelength is shifted to smaller wavelengths as a result of the non parallel light on the filter.
The combined spectra can now be transformed into a $g^{(2)}$ correlation function. The integral of the correlation function is the coherence time. The $g^{(2)}$ for IceAct are shown in Figure 4.27.

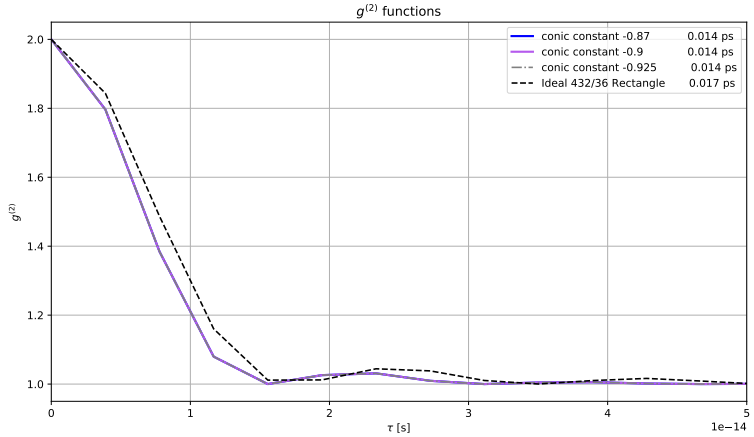

Figure 4.27: $g^{(2)}$ function for the IceAct with different conic constants

For the ideal rectangle the coherence time is 0.017 ps. The combined spectra of IceAct have a coherence time of 0.014 ps regardless of the conic constant. These short correlation times are explained by the large width of the bandpass filter, which is the inverse of the coherence time. It also shows that the light does not loose much coherence time with the used filter even if the rays are not parallelized at all.

4.3 Summary IceAct simulation

The interferometry setup for IceAct consists of less components than the one for H.E.S.S.. Its main part is the Fresnel lens SC 943 from Orafol. Other components, which are important for the simulation, are the interference filter and the PMT [15].
As a first step a spherical lens with focal length 502.1 mm and a clear aperture of 549.7 mm out of PMMA was calculated using Equation 4.1. The slope of this lens as well as Equation 4.4 was used to characterize the Fresnel lens (see Section 4.2.1). These data were then used to make the ray tracing simulation of the IceAct telescope. For refraction of the light at the lens Equation 4.9 was used. In addition to that a wavelength dependency of the refraction was implemented by determining the wavelength dependent refractive index $n(\lambda)$ via the Sellmeier equation 4.6.
For calculating the sagitta function (Equation 4.1) one parameter was still missing: the conic constant. In Section 4.2.2 the influence of this parameter is discussed as well some estimates of what the constants value is. These estimates were done by the measurement of the focal distance for a known wavelength as well as the statement of the manufacturer. The results were then compared to a measurement of the aberration radius by [28].
The angular distribution produced by the Fresnel lens was used to simulate a combined spectrum for IceAct using a interference filter with a width of 36 nm (see Section 4.2.3). These spectra where used to calculate the $g^{(2)}$-correlation function as well as the resulting coherence time of 0.014 ps.

5 Conclusion

Within this thesis ray tracing simulations were used and extended or in the case of the IceAct simulation build from scratch. The ray tracing for H.E.S.S. used the simulation data of previous conducted ROBAST simulations. These were integrated into to the simulation for the interferometry setup. In the scope of this thesis this framework was used to optimize the setup with a multitude of different variables. This variables were mainly the kind of the interference filter, the shift of the setup in regard to the telescopes focal point, the focal length of both the diverging and the converging lens and a stability against possible errors or inaccuracies in the pointing of the telescope. The optimization was done by systematically studying the influence of the changes in the setup on the measurement time and the coherence time. The changes on the measurement time and the coherence time were caused by the a combined spectrum that changed for altered AOIs. It showed that the optimal shift for the system is 1.5 cm. The measurement time for the three different filter revealed that the Alluxa 2 nm filter had the shortest time and the one for the Semrock 8.2 nm filter was a factor 1.52 times longer while the Thorlabs 10 nm had a measurement 1.15 times as long.
The result for best shift changed to 2.2 cm if instead of the diverging lens with a focal distance of -7.5 cm a lens with -6 cm is used. Then the optimal shift was achieved at 2.2 cm. The last setup proved to be superior if the offset in pointing can be held under 0.6 cm. An investigation in the size of the offset is needed.
The pointing accuracy plays a vital role in the decision of what converging lens is the optimal one. A bigger focal length for this lens proved to be beneficial, because more rays hit the PMT and the fraction of surviving rays rises. The optimal shift for longer focal distances was 2 cm shift. However the longer focal length is only of use if the offset is smaller than 0.5 cm. The simulation showed that in general the setup can be improved and how to do it, but it also shows that the offset is an issue that needs to be accounted for.

This thesis describes how the ray tracing simulations of IceAct were set up and what information was put in. It used basic geoemtric optics of parallel incoming light to characterize the behavior of the used Fresnel lens Orafol SC943. This behavior included an investigation for different wavelengths and the focal point at different distances.
One variable that needed further examination was the conic constant that was undetermined. The simulation could narrow down the size of the constant by using the given information, but a closer look on the constant could significantly improve the performance of the simulation to closer resemble reality.
The light produced in the ray tracing of the Fresnel lens was used to get a combined spectrum of the system. This enabled to calculate the $g^{(2)}$ correlation function and integrate it to get a reasonable estimate for the coherence time of the light measured with the IceAct setup, which is 0.014 ps.

The ray tracing simulations help gathering inside into the measurement setup to the point that optimization can be made. It also gives an estimate of the

performance of the whole system and helps predicting upcoming problems for the interferometry experiments.

List of Figures

List of Tables

List of abbreviations

H.E.S.S. The High Energy Stereoscopic System

IceAct The Ice Imaging Air Cherenkov Telescope

AOI angle of incidence

PMT photomultiplier tube

ROBAST ROot-BAsed Simulator for ray Tracing

CCD charge-coupled device

DAQ data aquisition

PMMA polymethylmethacrylate

FWHM Full width half maximum

ECAP Erlangen Centre for Astroparticle Physics

References

[1] John Davis. Forty years of progress in long-baseline optical interferometry: 2005 robert ellery lecture. *Publications of the Astronomical Society of Australia*, 23(2):94–104, 2006. doi: 10.1071/as06012. URL https://doi.org/10.1071/as06012.

[2] R Hanbury Brown, J Davis, and LR Allen. The angular diameters of 32 stars. *Monthly Notices of the Royal Astronomical Society*, 167(1):121–136, 1974.

[3] Advanced lab course (f-praktikum) experiment 45 photon statistics. https://www.fp.fkp.uni-erlangen.de/advanced-laboratory-course/selection-of-experiments/MSc-Versuchsanleitungen-englisch/B45E.pdf, Aug 2017.

[4] Wolfgang Demtröder. *Experimentalphysik 2 - Elektrizität und Optik*. Springer-Verlag, Berlin Heidelberg New York, 2017. ISBN 978-3-662-55790-7.

[5] D. Meschede. *Optics, Light and Lasers: The Practical Approach to Modern Aspects of Photonics and Laser Physics*. John Wiley and Sons, New York, 2017. ISBN 978-3-527-41331-7. URL https://books.google.de/books?id=MJCbCgAAQBAJ.

[6] Michelson stellar interferometer. https://commons.wikimedia.org/wiki/File:Michelson_stellar_interferometer.png, .

[7] Michelson stellar interferometer explanation. https://www.forphys.de/Website/qm/exp/v23.html, .

[8] R. Hanbury Brown, J. Davis, L. R. Allen, and J. M. Rome. The Stellar Interferometer at Narrabri Observatory—II: The Angular Diameters of 15 Stars. *Monthly Notices of the Royal Astronomical Society*, 137(4):393–417, 12 1967. ISSN 0035-8711. doi: 10.1093/mnras/137.4.393. URL https://doi.org/10.1093/mnras/137.4.393.

[9] W. Guerin, J. P. Rivet, M. Fouché, G. Labeyrie, D. Vernet, F. Vakili, and R. Kaiser. Spatial intensity interferometry on three bright stars. 2018. doi: 10.1093/mnras/sty1792.

[10] Oliver Stolz. *Differentielles Raytracing für spezielle Beleuchtungssysteme*. phdthesis, Friedrich-Alexander-Universität Erlangen-Nürnberg (FAU), 2010.

[11] The hess telescopes. https://www.mpi-hd.mpg.de/hfm/HESS/pages/about/telescopes/.

[12] Characteristics of the h.e.s.s telescopes. https://www.mpi-hd.mpg.de/hfm/HESS/pages/about/HESS_I_II/, 03 2021.

[13] The optical system of the h.e.s.s imaging atmoshperic cherenkov telescopes part ii: mirror alignment and point spread function. https://www.mpi-hd.mpg.de/hfm/HESS/pages/publications/others/hessopt2.pdf, 03 2021.

[14] Andreas Zmija. Intensity interferometry with H.E.S.S - Measuring angular diameters of stars.

[15] Hamamatsu r11265u series / h11934 series. https://www.hamamatsu.com/resources/pdf/etd/R11265U_H11934_TPMH1336E.pdf, Mar 2021.

[16] Wolfgang Demtröder. *Laserspektroskopie - Grundlagen und Techniken*. Springer-Verlag, Berlin Heidelberg New York, 2007. ISBN 978-3-540-33793-5.

[17] Alluxa optics website 465-2-od4 ultra narrow bandpass. https://www.alluxa.com/optical-filter-catalog/ultra-narrow-bandpass/465-2-od4-ultra-narrow-bandpass.html, Mar 2021.

[18] Interference filters. http://hydrogen.physik.uni-wuppertal.de/hyperphysics/hyperphysics/hbase/phyopt/intfilt.html.

[19] Mats G. Löfdahl, Vasco M. J. Henriques, and Dan Kiselman. A tilted interference filter in a converging beam. 2011. doi: 10.1051/0004-6361/201117305.

[20] 420/5 nm brightline single-band bandpass filter. https://www.laser2000.co.uk/product/ff01-420%C2%A75-25/420-5-nm-brightline-single-band-bandpass-filter, .

[21] Fbh450-10 thorlabs premium bandpass filter 450/10nm. https://www.thorlabs.com/thorproduct.cfm?partnumber=FBH450-10.

[22] Andreas Zmija. Design and characterization of an intensity interferometer with thermal light sources, Dec 2018. URL https://ecap.nat.fau.de/wp-content/uploads/2019/01/2018-AndreasZmija-MA-Intensity_Interferometry.pdf.

[23] Merlin Schaufel, Karen Andeen, and Jan Auffenberg. Iceact, small imaging air cherenkov telescopes for icecube, 2019.

[24] Semrock laser 2000 website ff01-432/36-25. https://www.laser2000.co.uk/product/ff01-432%C2%A736-25/432-36-nm-brightline-single-band-bandpass-filter, 03 2021.

[25] Hans Michael Eichler. Characterisation studies on the optics of the prototype fluorescence telescope famous. https://web.physik.rwth-aachen.de/~hebbeker/theses/eichler_master.pdf, Mar 2014.

[26] Tim Niggemann. New telescope design with silicon photomultipliers for fluorescence light detection of extensive air showers. https://web.physik.rwth-aachen.de/~hebbeker/theses/niggemann_master.pdf, Jan 2012.

[27] An illustration of various conic constants. https://commons.wikimedia.org/wiki/File:Conic_constant.svg, 08 2009.

[28] Tim Niggemann. *The Silicon Photomultiplier Telescope Famous for the Detection of Fluorescence Light*. phdthesis, RWTH Aachen University, Oct 2016.

[29] Orafol optic solutions website. https://www.orafol.com/de/europe/produkte/optic-solutions/produktlinien, Jan 2021.

[30] Maurice Günder. Simulation of the optics of the imagingair-cherenkov telescopes iceact with geant4, Apr 2019. URL https://git.rwth-aachen.de/tbretz/research/-/raw/master/Theses/Master/Maurice%20G%C3%BCnder%20-%20Simulation%20of%20the%20Optics%20of%20the%20Imaging%20Air-Cherenkov%20Telescope%20IceAct%20with%20Geant4.pdf.

[31] refractive index of pmma. https://refractiveindex.info/?shelf=organic&book=poly(methyl_methacrylate)&page=Sultanova.

[32] 432/36 nm brightline single-band bandpass filter. https://www.laser2000.co.uk/product/ff01-432%C2%A736-25/432-36-nm-brightline-single-band-bandpass-filter, .

Appendix

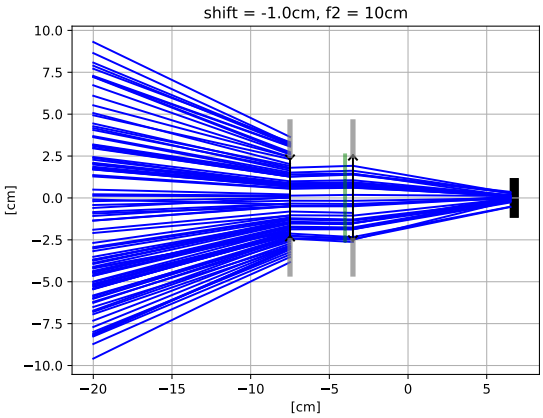

Figure 1: Ray propagation for a setup with a shift of -1.5 cm to the original setup and the H.E.S.S. focal point

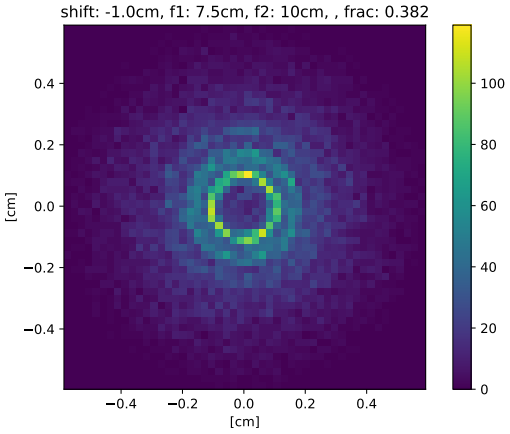

Figure 2: Focal spot for the a setup with -1 cm shift to the inital setup

Statutory Declaration

I declare that I have developed and written the enclosed Master's Thesis completely by myself, and have not used sources or means without declaration in the text. Any thoughts from others or literal quotations are clearly marked. The Master's Thesis was not used in the same or in a similar version to achieve an academic grading or is being published elsewhere.

Place, Date	Signature

Acknowledgements

During my work on this thesis I received great support from people who I want to thank:

- **Prof. Dr. Stefan Funk** for providing me with this interesting topic, the opportunity to be part of the AQO research group and his guidance regarding structure and focus topics of the thesis
- **Prof. Dr. Gisela Anton** for her expertise in meeting discussions and sharing her thoughts.
- **Andreas Zmija** for his patient support, for the organization of the AQO meetings, for his excellent feedback and the fun regular Wednesday virtual calls that I enjoyed a lot and will for sure miss.
- **Alisa Helldörfer** for always encouraging me and making my day bright.
- **My family Hans, Heike and Miriam Konrad** for always supporting me and enduring my extensive physics talks during dinner.